Modelling the Water Table in a Bog

Tobias Bowley

Supervised by Veiko Lehsten and Moa Sporre

Department of Physics and Department of Physical Geography

June 19, 2023

LUND UNIVERSITY

Acknowledgements

Abstract

Over the past five years, an ongoing study at INES, Lund University, have examined the encroachment of trees and vegetation into a bog ecosystem in northern Scania, Sweden. While several factors have been identified as contributing to this ecological transformation, including, nutrient availability, and climate, the hydrological aspect remains a key area of investigation. This thesis aims to deepen our understanding of how the groundwater table in the bog changes over time in response to various environmental factors.

To achieve this aim, extensive fieldwork was conducted during the late winter and early spring, during 2023, to measure the water table and gather data on rainfall and evapotranspiration. The measurements were taken using a combination of manual techniques, such as pressure transducers, and automated data loggers. These measurements were then combined with existing data on the bog's hydrological regime, as well as data from SMHI (Sveriges meteorologiska och hydrologiska institut) covering the local area, to create a model of the groundwater table.

The model revealed several important insights into the hydrological dynamics of the bog. Firstly, it showed that the water table responds rapidly to rainfall, with a sharp increase in water levels observed following periods of heavy precipitation. Additionally, there is also occasionally an unknown source pushing the water tables to even higher levels. Secondly, it demonstrated the importance of evapotranspiration in regulating the water balance of the bog. Thirdly, it revealed a steady rate of water runoff, indicating that the bog acts as an important water regulator for the surrounding landscape.

These findings have important implications for the management and conservation of bogs and wetland ecosystems. The model created in this thesis allows forecasting of fluctuations in the groundwater table through numerical analysis of the given data, thus enabling the tracking of water table changes. Furthermore, the model can be adapted for use in other bogs and wetlands with minor adjustments, providing a valuable tool for future research in this field.

Popular Science

Water flow has been studied for decades by scientists in many fields of natural science for many reasons. It is necessary to have a solid understanding of physics, such as classical mechanics and fluid dynamics and have passed a number of levels in university mathematics in order to comprehend the movement of water.

Peat often develops as a result of incomplete decomposition of vegetation that grows in waterlogged environments. This is a result of either standing water, such as lakes or the edges of slow-moving watercourses, or areas that have consistently received heavy rainfall. Partially decomposed plant debris builds up and becomes densely compacted, which causes peat to form and alter the substrate's chemical composition and physical characteristics. Peatlands or mires are the names for these ecological systems.

Peat typically forms when less organic matter is lost through decomposition than is gained through photosynthesis. The vegetation succession that results is known as hydrosere. Although these ecosystems are found all over the world, the Northern Hemisphere is where they are most prevalent. Fluid dynamics, hydrology, and chemistry have a significant influence on studies of peatlands. These ecosystems are also closely related to studies in biodiversity and vegetation.

Bogs and fens are two different types of peatlands. Although the two types of wetlands are very similar to one another, what sets them apart from is where they get their water from. While bogs are enclosed and only supplied with water by precipitation, fens are typically supplied with water from the ground water flow.

Long-term global climate change means that ice ages and their counterpart, interglacials, occur in even intervals over thousands of years. We are currently in the heating phase, the interglacial part, of this naturally occurring cycle. However, the global emission of greenhouse gases has been rising dramatically since the industrial revolution in the early 20th century, which raises the global temperature and affects all life on Earth. This subsequently leads to the unavoidable interglacial potentially peaking with a lot higher temperatures than without the influence of anthroprogenic presence.

This project focuses on vegetation encroaching on mires. The mire in question is known as Fäjemyren and is referred to as a bog. It is situated in the northern part of Scania, Sweden. One might anticipate that there will be few to no trees growing here because there are no nutrients added to it other than what is found in the precipitation. In some regions of Europe, the precipitation contains enough nitrogen and phosphor to supply bogs and fens with the minerals the vegetation need to flourish. Studies show a decline in these minerals in the precipitation in the majority of Scandinavian regions, dating as far back as the middle of the 20th century. Despite this decline, trees began moving in at Fäjemyren sometime in the 1960s, and as a result, the bog has lost up to 200 meters of wetland to forest.

Numerous factors, not to mention the fact that farmers turned peatlands into agricultural fields in the late 1800s and early 1900s, could have an impact. Could it be that climate change is to blame for the longer droughts, which helps the tree seedlings' root systems to grow sufficiently and become hardy enough to withstand subsequent rainy periods?

The study at Fäjemyren explores various topics, and this thesis specifically focuses on developing a model to predict changes in groundwater levels over time. These changes are influenced by factors that vary daily and seasonally, such as rainfall, evaporation, water uptake by plants, and water runoff. By using data collected from instruments at the research site and information from the Swedish Meteorological and Hydrological Institute, it is indeed possible to make these predictions. Of course, the predictions aren't perfect, as no data collection is ever flawless, whether it's done by machines or humans. This model allows us to understand water flow in the area and might even spark a conversation about a possible fifth unknown factor contributing to the water supply in the bog.

Contents

1. Introduction

When the decomposition of vegetation growing in waterlogged conditions is incomplete, the remains often form peat. This is a result happening in both standing water (meaning lakes or margins of slow flowing water courses) or areas being exposed to consistent high rainfall. Remains of vegetation which is partially decomposed accumulate and become densely compact, hence leading to peat formation which in turn alters the substrate's chemical composition and physical properties ("Peat Formation", 2019). These ecosystems are referred to as peatlands or mires.

Generally, peat is formed when the loss of organic matter is less via decomposition, than that produced through photosynthesis (Fath, 2018). This resulting vegetation succession is referred to as hydrosere.
While these ecosystems can be found around the world, they are most common in the Northern Hemisphere. Needless to say, fluid dynamics, hydrology and chemistry are big influential areas in the studies of peatlands. They are also strongly associated with biodiversity, flora and vegetation (Fath, 2018).
Peatlands, or mires, occur as two different types: bogs and fens. Although the two types are very similar types of wetlands, what makes them different from each other is the source of their water supply. While fens typically has a stable source of water through the ground water, bogs are enclosed and are solely fed water by precipitation (Sjörs, 1959).

The climate of the planet is fluctuating over time, meaning that it passes through ice ages and its counterpart, interglacials. This is a naturally occurring cycle and we are currently in a heating phase which ultimately will lead to a peak in the interglacial (Lindsey & Rebecca, 2022). However, with the industrial revolution during the, beginning early 20th century, the globally emitted green house gases has been increasing dramatically which has boosted the heating process dramatically and is affecting all life on Earth, thus affecting ecosystems such as peatlands.

The research of this project focuses on vegetation overtaking mires. The name of the mire which is focused on is Fäjemyren, which is defined as a bog and is located in northern Scania (Sweden). Since there are no nutrients fed to this, except of that which is in the precipitation, one could expect little to no trees at all growing here. In some parts of Europe the amount of nitrogen and phosphor in the precipitation is high enough to provide bogs and fens with minerals for the trees to thrive (Verhoeven et al., 1990), still in most parts of Scandinavia studies shows a decline in these minerals in the precipitation, as far back as the mid 1900s (Moore Jr. & Miller, 1994). Despite the observed decline, tree encroachment has been occurring at Fäjemyren since the 1960s, resulting in the loss of up to 200 meters of wetland, from the edge of the peatlnd, to forested areas.

There are anthropogenic factors that may contribute to this, including the conversion of peatlands to agricultural fields during the late 19th and early 20th centuries (Berglund, 2000). This is someting that happened all over Sweden.

The issue of the encroachment subject if an ongoing research project at INES (Lund University), co-led by Veiko Lehsten, which investigates the hypothesis that climate change-induced longer drought periods enable tree seedlings to develop robust root systems, allowing them to withstand subsequent rainy periods.

This research project has been subdivided into distinct branches, one of which centers on investigating the response of the groundwater table in the bog to rainfall patterns. This branch aims to explore the mechanisms of rainwater absorption by the peat substrate, the rate of flow of water away from the bog, and the contribution of evapotranspiration processes to these hydrological processes. These questions are central to the research objectives of this thesis. Through the utilization of diverse meteorological information, an endeavor is undertaken to construct a model aimed at replicating the observed fluctuations in the water table.

2. Method and Equipment

The location of the area of investigation at Fäjemyren is 56°15'47.5"N, 13°32'58.4"E (WGS84), which is the southern most area of the bog as a whole. Fäjemyren has a total area of roughly 2 km^2, whereas the INES research area covers roughly 0.21 km^2 of land (Figure 1a). Due to the complexity when carrying out the creation of a computational models, such as this one, it is necessary to initially start by delimiting the changing variables. When carrying out calculations on ecosystems, it becomes most representative when not simplifying it too much. The water flow varies a lot depending on the soil. For this model, only the green area labeled "Study area" (Figure 1) was selected for the calculations. This is because obtaining updated parameters for stomata in various forest-dwelling flora is currently unattainable, in addition to requiring intersecting measurements for non-peat soil permeability. By employing Lantmäteriet's data and comparing the soil type layer with satellite imagery, an accurate estimation of the tree encroachment and soil transitions can be achieved, thus justifying the focus on the study area.
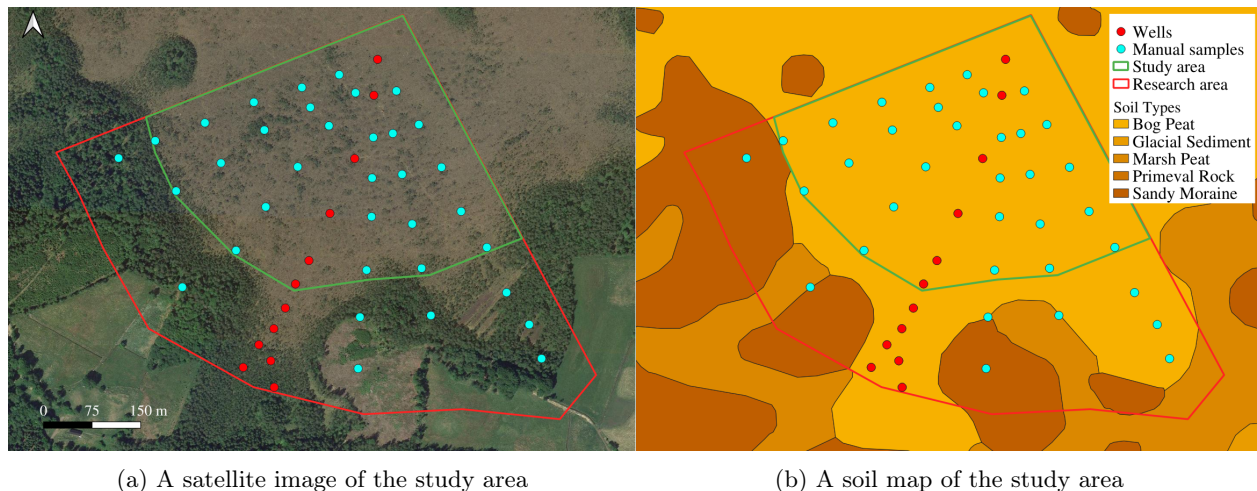

(a) A satellite image of the study area   (b) A soil map of the study area

Figure 1: Maps showing the delimitations of the area. Loggers (red dots) from the top: **1**. HOBO 20796674, **2**. ReefNet 15617, **3**. ReefNet 15592, **4**. ReefNet 15606, **5**. ReefNet 15543, **6**. HOBO 20796679, **7**. ReefNet 15610, **8**. ReefNet 15566, **9**. ReefNet 15566, **10**. HOBO 20796630, **11**. ReefNet 15585, **12**. ReefNet 15545. Source of layers: Lantmäteriet

Typical for a bog in this region is a bottom consisting of a mineral soil composed of sand, silt and clay particles. The peat soil is almost completely saturated, with a saturation level greater than 95% and the depth of the soil fluctuates through out the bog with measurements varying with meters across the bog. The area is mainly covered in a variety of heather (Figure A1, A2) and short grass plants (Figure A3) and only a few tree species spread around; mostly scotts pine and birch. Despite the age of the trees, some as old as 60 years (Figure A4, A5), their vertical growth remains stunted, reaching no more than a few meters above the ground level (FigureA6, A7). This observation indicates that the soil's nutrient availability is substantially restricted, impeding the possibility for greater plant growth, thus proving the soil's nutrient deficiency in a bog. Fäjemyren is situated at an elevation of around 142-144 meters above sea level. The temperature of the water spans between 5 ^oC and 10 ^oC, with occasional fluctuations outside the range.

The methodology employed for obtaining measurements primarily involves the utilization of fixed instrumentation, the data from which are acquired on site, as there are no remotely surveyed instruments. To ensure the reliability and validity of the measurements, manual readings are also conducted alongside the instrumental measurements. A weather station has been operational since 2015, continuously recording pertinent meteorological parameters. In 2019, supplementary hydrological monitoring devices were installed to further enhance data collection. Subsequently, in 2021, a selection of these devices was upgraded to more advanced

logging instruments to maintain contemporary data acquisition standards.

During a typical day in the field, carrying out measurements and readings generally takes approximately four hours, depending on weather conditions. Given that navigating the terrain is akin to traversing a colossal sponge (Figure A8), the physical demand warrants intermittent short breaks, thereby extending the duration of the stay.

In order to ascertain the depth of the water table, a variety of scientific instruments and apparatus are employed to monitor fluctuations in pressure. The ensuing section will expound on the specific equipment utilized during this investigation and detail the methodology for their application.

2.1. "The Spear", the water probe and the GPS

The so called Spear, a versatile handmade instrument, serves to facilitate the measurement of subsurface water levels. Comprising a hollow shaft with a pedal, this device allows for the penetration of the soil with foot-induced force, reaching the underlying aquifer. Additionally, a small platform positioned at the pinnacle of the shaft enables the attachment of a GPS device to obtain precise x, y, and z coordinates of the measurements (Figure A9).

After the spear has been firmly secured in the ground, the water probe is subsequently lowered down the shaft, and upon initial contact with the water, an audible alarm is promptly triggered. From reading the length units on ribbon to which the probe is attached, the depth can be determined. The probe device name is *ELWA PLS 15* (Figure A9) and detects the water level based on the principles of electrical conductivity. The probe of the device contains two electrodes, which are separated by a small gap. When the probe is lowered into the spear and reaches the water level, the water completes the electrical circuit between the two electrodes (*PLS 15-20*, 2013).

Once the water level is recorded, the GPS data is obtained using a remote PC connected to the GPS device via Bluetooth (Figure A10). Acquiring satellite signals can occasionally be a time-consuming process, depending on the terrain. In open fields, the connection typically establishes within seconds, whereas obtaining a signal in densely vegetated or forested areas may require waiting for several minutes.

GPS devices determine location by receiving signals from satellites orbiting Earth, which continuously broadcast their position and time data. Generally, with $d = t \cdot c$, the distance is determined. The d is the distance between the device and the satellite, t is time in seconds and c is the speed of light in vacuum (Kaplan & Hegarty, 2017).

The device used in the research is a HiPer HR, developed by Topcon. The Topcon HiPer HR, a high-performance GNSS receiver, is designed for surveying, construction, and geospatial experts. Equipped with 452-channel Vanguard Technology, the HiPer HR tracks and processes signals from all satellite constellations, maximizing performance in challenging environments like urban canyons or dense tree coverage. Its integrated inertial measurement unit enables tilt compensation and quick initialization, reducing the need for precise leveling during setup. The device also features advanced fence antenna technology, minimizing multipath interference and improving accuracy. Real-Time Kinematic corrections provide real-time centimeter-level accuracy for surveying and mapping. Lastly, the HiPer HR supports multiple satellite constellations, such as GPS, GLONASS, Galileo, BeiDou, QZSS, and SBAS, ensuring improved accuracy, signal availability, and redundancy in challenging conditions or during system disruptions (Topcon, 2016).

The error margin can vary depending on factors like satellite visibility, signal quality, and environmental conditions. In optimal conditions with clear line-of-sight to the sky and minimal obstructions, the accuracy is generally at its best. The uncertainty is read on the display of the reader and at optimal levels on site it varies between $\pm 1.3\ cm$.

2.2. Water Level Loggers

To retrieve data from the loggers, they are pulled up from the wells (Figure A11) and connected to a PC (Figure A12). The accompanying software for the device is used to generate a CSV file containing the data. Simultaneously, manual measurements using a ruler are taken with the well lid removed (Figure A13). These manual measurements are needed for estimating the direction of the water flow, the runoff rate of the water flow and to varify the logger measurements.

The *HOBO U20* Water Level Logger and the *Reefnet Sensus Ultra* are both water logging instruments which are used to continuously monitor the water levels (Figure A14).

The HOBO U20 has a measurement range of up to 9 m. It has a measurement accuracy of $\pm0.1\%$ full scale, which translates to a maximum potential error of ±0.009 m for a full scale water level measurement. The U20 also includes a temperature sensor to compensate for temperature changes, which can affect the accuracy of water level measurements (*U20 Water Level*, 2018).

The Reefnet Sensus Ultra has a much larger measurement range of up to 200 m. It has a measurement accuracy of $\pm0.05\%$ full scale, which translates to a maximum potential error of ±0.1 m for a full scale water level measurement (*SENSUS ULTRA*, 2018).

Both instruments measures the water level by measuring the pressure with a piezoresistive pressure sensor, which are, due to their elastic nature, compensated for changes in the water temperature to ensure accurate water level measurements. The density of water changes when the temperature changes, and this change in density is directly proportional to the pressure.

A piezoresistive pressure sensor works based on the principle of piezoresistivity, which refers to the phenomenon of changes in electrical resistance of a material in response to mechanical stress. Piezoresistive pressure sensors typically consist of a pressure-sensitive material, which is usually a semiconductor, such as silicon or germanium, that is doped with impurities to create areas of either excess or deficient electrons. The pressure-sensitive material is typically formed into a thin diaphragm, which deforms under the influence of pressure. When the diaphragm is deformed by pressure, the spacing between the impurity atoms in the semiconductor lattice changes, which alters the number of free electrons available for conduction in the material. This change in electron density leads to a change in the material's resistance, which is then detected as a change in voltage across the sensor. The magnitude of the voltage change is proportional to the amount of pressure applied to the diaphragm. By measuring this voltage change, piezoresistive pressure sensors can accurately measure pressure (Staib, 2015).

According to the HOBO U20 manual, the instrument may experience a drift of up to 0.2% full scale per year. To minimize the risk of drift, the manual recommends recalibrating the instrument at least once per year, or more frequently if the instrument is deployed for extended periods of time or in harsh environmental conditions (*U20 Water Level*, 2018). Similarly, the Reefnet Sensus Ultra manual acknowledges the potential for drift to occur in the pressure sensor over time, and recommends regular calibration and maintenance to ensure the accuracy of water level measurements (*SENSUS ULTRA*, 2018).

2.3. The Weather station

The on-site weather station acts as a sophisticated meteorological data collection system, designed to acquire a wide range of atmospheric information (Figure A15). Although it contains numerous instruments, only few are relevant to this specific research. The station is connected to a computer, and data is accessed by removing a CF-card and copying its contents, which must be reformatted due to their unique structure.

This research primarily focuses on the sensors and the devices that measure radiation, humidity, water temperature, air temperature, and air pressure. Additional atmospheric data, such as precipitation and wind speed, are sourced from the Swedish Meteorological and Hydrological Institute's (SMHI) publicly available database (SMHI, 2023) and integrated into the study. This information is gathered from two nearby stations, Bjärnum and Hästveda, both within 23 *km* of the bog. While the Bjärnum SMHI station (which is within

10 km) provides wind measurements, it lacks information about precipitation, hence the need of data from the Hästveda SMHI station as well.

2.3.1. Vaisala PTB210

The *Vaisala PTB210* barometric pressure sensor is employed for the quantification of atmospheric pressure. This instrument is characterized by its high precision, with an uncertainty margin of ± 0.3 hPa. Similar to HOBO U20 and ReefNet Sensus Ultra, the Vaisala PTB210 utilizes a piezoresistive pressure sensor for its measurements (Vaisala, 2021).

2.3.2. Rotronic MP102H

To measure the realtive humidity *Rotronic MP102H* uses a capacitive humidity sensor, with an accuracy of ± 1.7 %. These sensors operates based on changes in capacitance resulting from the interaction between a dielectric material and water vapor in the surrounding environment (Technologies, 2011). Capacitance (C) can be described using the formula:

$$C = \epsilon \cdot \frac{A}{d},\tag{1}$$

where ϵ is the dielectric constant of the material, A is the area of the conductive plates, and d is the distance between the plates (Figure 2).
The change in capacitance is proportional to the change in humidity, allowing the sensor to provide a measurement of relative humidity.

With an acuracy of ± 0.1 ^{o}C the Rotronic MP102H uses a Pt100 resistance temperature detector (RTD) to measure the temperature (Technologies, 2011). The sensing element in an RTD is made of a thin platinum wire, which is chosen due to its high stability, nearly linear temperature-resistance relationship, and low electrical noise. Platinum also exhibits excellent corrosion resistance, making it suitable for various environmental conditions (ProcessParameters, 2023). The electrical resistance of the platinum wire changes as a function of temperature. This change in resistance is primarily due to the increased thermal motion of electrons and lattice vibrations within the material as the temperature increases. These factors lead to an increase in the resistivity of the material and, subsequently, the resistance of the wire. Stating the resistance $R(T)$ as a function of temperature:

$$R(T) = R_0(1 + \alpha \cdot T)\tag{2}$$

R_0 is the resistance at 0 ^{o}C (for a Pt100, $R_0 = 100$ ohm). The α is the temperature coefficient of resistance (for platinum, α is approximately $0.00385^{o}C^{-1}$). This linear approximation works well for relatively small temperature ranges (Childs, 2001).
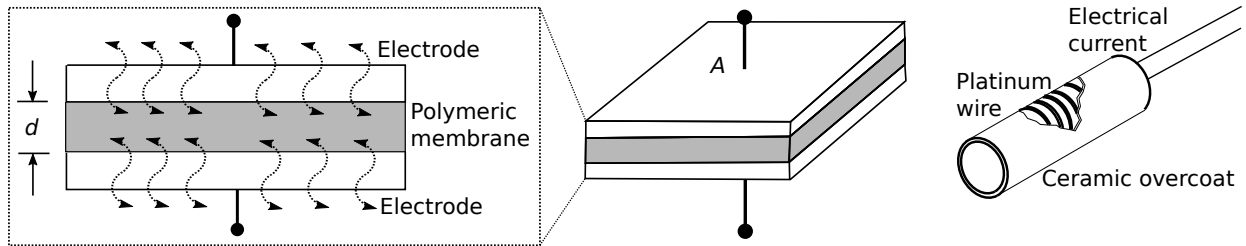

Figure 2: Anatomy of the Rotronic MP102H sensors. To the left the capacitive humidity sensor. To the right the Pt100 resistance temperature detector

2.3.3. Kipp & Zonen CNR 4

Kipp & Zonen CNR 4 is the name of the instrument which measures the net radiation as

$$R_n = (R_{s_{inc}} - R_{s_{ref}}) - (R_{l_d} - R_{l_u}), \tag{3}$$

where $R_{s_{inc}}$ and $R_{s_{ref}}$ is the incoming and reflected short wave radiation, respectively, and R_{l_d} and R_{l_u} is the downwards facing and upwards facing long wave radiation, respectively. The sensor measuring the short wave radiation flux is a pyranometer with an error margin of $\pm 10 \ Wm^{-2}$, detecting radiation in the 0.3 to 2.8 μm range. The sensor for detecting the long wave radiation flux is a pyrgeometer with an error margin of $\pm 20 \ Wm^{-2}$, detecting radiation in the 4.5 to 42 μm range (Klip&Zonen, 2015).

A pyranometer measures global solar radiation using a thermopile placed beneath a blackened sensing surface that absorbs solar radiation uniformly across the entire solar spectrum. The sensing surface is covered by a transparent dome that protects it from external influences and ensures a cosine response to incoming radiation. As the sensing surface absorbs solar radiation, it heats up, creating a temperature difference between the hot and cold junctions of the thermocouples in the thermopile. This temperature difference generates a voltage proportional to the absorbed radiation due to the Seebeck effect, which is a manifestation of thermoelectric phenomena originating from the redistribution of charge carriers (electrons or holes) in the presence of a temperature gradient. At a quantum level, the temperature difference causes a change in the electron distribution across the junctions, resulting in a voltage difference. The voltage is then amplified and converted into an electrical signal proportional to the solar radiation, which can be recorded by a data logger or monitoring system. The pyranometer is calibrated using a reference standard to ensure accuracy in field measurements (Kipp&Zonen, 2015). What makes a pyrgeometer different from a pyranometer is to which sensitivity the device is set. Normally the protective glass is made of different materials, in which it allows selected wave lengths of the electromagnetic spectra to pass through. The coating also posses varying features.
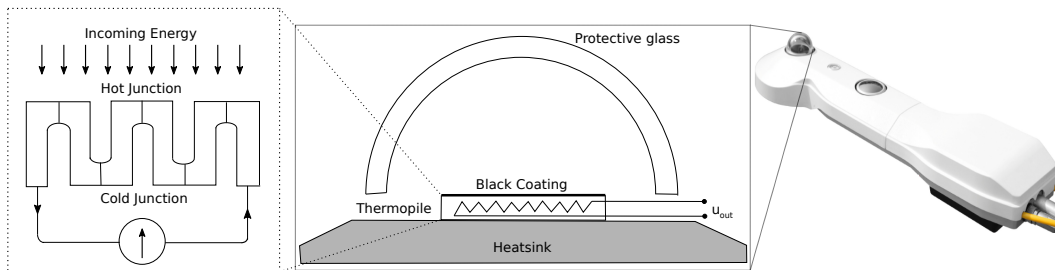

Figure 3: The anatomy of a pyranometer and a pyrgeometer

2.4. Data Acquisition and Analysis

After collecting the data, it was subjected to analysis using Python as the principal tool. Utilizing various modules, the data is organized, processed, and visualized. Each dataset from the individual devices and the data from SMHI, has its own distinct format. Notably, some datasets employ imperial measurements, necessitating conversion to metric units. The Pandas module plays a leading role in consolidating the various datasets into a unified data frame with a consistent structure. For numerical analysis and processing, the Numpy module is predominantly employed. Lastly, data visualization is achieved through the use of the Matplotlib module, which facilitates the creation of informative plots to effectively represent the findings.

During the examination of maps and interpolation of areas, QGIS software was employed as the principal tool. Built on Python, QGIS offers a user-friendly graphical interface and the capability to write and apply code to maps, making it a highly versatile and potent instrument. In this study, QGIS is primarily used to generate a vector field for visualizing water flow patterns. The map layers utilized in this research are

sourced from Lantmäteriet, the Swedish Land Survey authority. These layers provide essential geospatial information, enabling accurate analysis and interpretation of the study area.

3. Modelling and Theory

The water balance equation is a fundamental tool used in hydrology to quantify the inputs, outputs, and storage changes of water within a system, such as a peatland. This equation provides a simplified representation of the complex hydrological processes that govern water movement and storage in these ecosystems. The basic water balance equation for a peatland can be expressed as:

$$\Delta h = P_h - ET_h - Q_h \tag{4}$$

Where Δh represents the change in the height of the water table (m/s), P_h denotes precipitation (m/s), ET_h stands for evapotranspiration (m/s), and Q_h refers to runoff (m/s). The water balance equation assumes that the peatland is a closed system, and it provides a starting point for estimating the change in the water table.

3.1. Precipitation

Rainfall plays a crucial role in determining fluctuations in the water table since it directly influences the quantity of water available for replenishment. In a bog ecosystem, where the ground is saturated, the extent of rainfall corresponds to the variation in the water table's elevation. In peatlands, where the soil is almost entirely saturated, precipitation can be considered a consistent source contributing to the rise in groundwater levels (Holden, 2005). The unique soil composition, consisting predominantly of partially decomposed plant matter, grants peatlands a remarkable water-retention capacity. This causes the soil to be near close to fully saturated, and any further rainfall can help elevate the groundwater table (Limpens, Berendse, Blodau, Canadell, et al., 2008). An analogy for peatlands could be that they function like sponges, holding and retaining water, and any additional moisture they absorb contributes to raising the overall water level (Figure A8). In situations not involving peatlands, additional factors need to be taken into account, like the soil's infiltration rate (I) and its hydraulic conductivity (k_h). The I and the k_h are vertically dependent on the depth of the soil before reaching water table below. This results in the following equation:

$$\Delta P_h = (P \cdot I)/(k_h \cdot A), \tag{5}$$

However, when the soil saturated and the assuming that the rainfall is uniformly distributed across the area; $A = 1$, the change in the water table can be simplified to:

$$\Delta P_h \equiv P, \tag{6}$$

meaning that the amount of rain is equivalent to the positive change in the water table in a the bog (Dingman, 2015).

3.2. Evapotranspiration

The Penman-Monteith equation (PME) is a complex and widely used method for estimating evapotranspiration (ET) that combines energy balance and aerodynamic concepts. It was developed through the combination of the original Penman equation (Howard Penman, 1948), whose focus was on evaporation, and the work of John Lennox Monteith, which incorporated the effect of stomatal resistance and transpiration on ET (Monteith, 1965):z

$$ET = \frac{\Delta(R_n - G) + \rho_a c_p(\delta_e)g_a}{(\Delta + \gamma(1 + g_a/g_s))L_v}, \tag{7}$$

where Δ is the rate of change of saturation specific humidity with air temperature (PaK^{-1}), R_n is the net radiation (Wm^{-2}), G is the ground heat flux (Wm^{-2}), ρ_a is the dry air density (kgm^{-3}), c_p is specific heat capacity of air ($Jkg^{-1}K^{-1}$), δ_e is vapor pressure deficit (Pa), g_a is the atmospheric conductance (ms^{-1}), g_s the conductivity of stomata ($ms-1$), γ is the psychrometric constant (PaK^{-1}) and L_v is volumetric latent heat of vaporization (Jm^{-3}). R_n is the net radiation and is taken from measured data from the weather station on site. The value for ρ_a is 1.352 kg/m^3, the dry air density, which, in this case, this value is taken from a table (Engineering-ToolBox, 2003). The value for latent heat of vaporization (λ_v) at the range of water temperature, which spans between 5 ^oC and 10 ^oC is roughly 2484.3 kJ/kg (Engineering-ToolBox, 2010).

3.2.1. The Rate of Change of Saturation Specific Humidity (Δ)

The rate of change of saturation specific humidity with air temperature is calculated by

$$\Delta = \frac{\partial P_{sa}}{\partial T} = \frac{P_{sa} \cdot H_L(T)}{c_p \cdot T^2}, \tag{8}$$

where P_{sa} is the saturation vapour pressure (Pa) and is calculated from the empirical formula Magnus-Tetens equation (Lowe & Ficke, 1974):

$$P_{sa} = A_{sa} \cdot exp\left[\frac{B_{sa} \cdot T}{C_{sa} + T}\right]. \tag{9}$$

The A_{sa}, B_{sa} and C_{sa} are all empirical constants derived from experimental data. A_{sa} has a value of 611.21 Pa and is a scaling factor that adjusts the overall magnitude of the saturation vapor pressure. B_{sa} is dimensionless and has a value of 17.502. It controls the temperature dependence of the exponential term in the equation. C_{sa} is also dimensionless, with a value of 240.97 and acts as a temperature scaling factor and helps to set the temperature range over which the equation is most accurate (Murray, 1967).

H_L is the latent heat of vaporization of water, which in our case, is roughly $2.5 \cdot 10^6$ Jkg^{-1} and is calculated by

$$H_L(T) = A_L - B_L \cdot T + C_L \cdot T^2 - D_L \cdot T^3. \tag{10}$$

The constants A_L, B_L, C_L and D_L are all constants derived from Gnielinski's work (Henderson-Sellers, 1984). A_L has a value of 2500.8 $kJkg^{-1}$ and is an approximation of the latent heat of vaporization at 0°C. B_L is equal to 2.36 and is a dimensionless linear coefficient that represents the rate of change of the latent heat of vaporization with respect to temperature. C_L has a value of 0.0016 $kJkg^{-1}T^{-2}$ and is a quadratic coefficient that represents the curvature in the temperature dependence of the latent heat of vaporization. Finally D_L is a cubic coefficient that represents higher-order changes in the temperature dependence of the latent heat of vaporization and has a value of 0.00006 $kJkg^{-1}T^{-3}$.

Last in the equation for rate of change of saturation specific humidity with air temperature is c_p is, again, an empirical value. It is estimated from the following expression:

$$c_p = \frac{Q}{m\Delta T}, \tag{11}$$

where Q is the energy (J), m is the mass (kg) and ΔT is the change in temperature. Without having any experimental values for the mass of the air parcel, nor the energy needed to estimate a value for c_p, one has to refer to predetermined tables. In this case the value of c_p is approximately 1005.8 $Jkg^{-1}K^{-1}$ (Urieli, 1984)(Engineering-ToolBox, 2004).

3.2.2. The Ground Heat Flux (G)

Stating the expression for calculation of the ground heat flux (G):

$$G = \frac{\partial T}{\partial z} = k_c \cdot \frac{\Delta T}{l_y}. \tag{12}$$

The thermal conductivity is denoted by k_c and is low as peat moss has a lower thermal conductivity than typical mineral soils due to its high organic matter content and low bulk density. In peat moss the thermal conductivity is approximately 0.445 W/mK with an error margin of ± 0.045 W/mK (Kujala et al., 2008). The change in T is that which is between the soil temperature and the air temperature and l_y is the depth of the point where the soil temperature is taken. The depth l_z is 0.5 m and has an uncertainty level of ± 0.1 m.

3.2.3. Vapor Pressure Deficit (δ_e)

The vapor pressure deficit represents the discrepancy between the saturation vapor pressure at a given air temperature and the actual vapor pressure of the air. Measured in Pascals, it is a pressure unit and is influenced by relative humidity. This metric is significant as it serves as an impetus for evaporation from the Earth's surface into the atmosphere (Baldocchi, 2014). The formula for calculating the vapor pressure deficit is stated by

$$\delta_e = P_{sa} \cdot T \cdot (1 - H_r), \tag{13}$$

where H_r is the relative humidity.

3.2.4. The Atmospheric Conductance (g_a)

Conductivity of air, atmospheric conductance, is directly linked to the aerodynamic resistance for a reference surface (r_a) and is stated by

$$g_a = \frac{1}{r_a} \rightarrow r_a = \frac{ln\left(\frac{z_t - d}{z_{om}}\right) \cdot ln\left(\frac{z_t - d}{z_{oh}}\right)}{k_v^2 \cdot u}. \tag{14}$$

In the estimation of the aerodynamic resistance the z_t is 2 m and is the reference height of the weather station at the site. The zero-plane displacement height (d) is the height above the surface at which the wind speed is effectively zero due to the presence of roughness elements such as vegetation. This can be estimated at $\frac{8.5}{12}$ of the surrounding vegetation height. A rule of thumb, regarding d is of an error margin on d is $\pm \frac{0.5}{12}$ (Graf et al., 2014). The vegetation height of the area (z_v) varies between zero and 0.6 m, hence setting the error margin for the vegetation at ± 0.295 m. The k_v is the von Kármán constant, a dimensionless constant at 0.4, with an error margin of ± 0.02 (Bailey et al., 2014). The u denotes the wind speed.

The parameter z_{oh} is the roughness length governing transfer of heat and vapour (m) and z_{om} is the roughness length governing momentum transfer, can be estimated from the crop height (m).
In order to get a good approximation for z_{oh} and z_{om} the decision to employ the widely recognized FAO56 Penman-Monteith equation (FAO56), a standardized version of the original PME, was made. Developed by the Food and Agriculture Organization (FAO), this equation calculates reference ET for a hypothetical reference crop with distinct characteristics, including being well-watered, actively growing, and covered in short green grass. Notable similarities exist between the reference ecosystem in FAO56 and a peatland. Both settings exhibit well-watered conditions, ongoing plant growth, and short vegetation (Pereira et al., 2015). The FAO56 vegetation height falls within the range observed in peatlands, and the albedo measured at the weather station on site aligns with that of agricultural land (Schaeffer et al., 2006). Referring to FAO56 z_{om} can be determined by $0.123 \cdot z_v$ and z_{oh} subsequently by $0.1 \cdot z_{om}$.

3.2.5. The Conductivity of Stoma (g_s)

The stomatal conductivity is directly related to the bulk of of the growing vegetation (r_s) and can be written as

$$g_s = \frac{1}{r_s} \rightarrow r_s = \frac{r_l}{L_a}, \tag{15}$$

where r_l is the stomatal resistance of a single leaf, which, according to FAO56 (Allen et al., 1998), measures about 100 s/m under well-watered conditions. The Leaf Area Index (L_a) is a unitless measure representing the ratio of leaf surface area (only the top side) to the corresponding ground area beneath it, usually denoted in m^2 of leaf area per m^2 of ground area. The active L_a refers to the portion of the leaf area that actively participates in heat and vapor exchange processes, typically found in the sunlit upper section of a dense plant canopy (Allen et al., 1998). Deriving L_a:

$$z_v \cdot 12 = L \rightarrow L \cdot 0.5 = L_a. \tag{16}$$

12 is an empirical factor used to account for the daily cycle of sunlight and the proportion of the canopy that is sunlit. 0.5 represents the proportion of the canopy that is considered active. This assumption simplifies the calculation by assuming that only the top 50% of the grass is actively involved in the heat and vapor transfer (Allen et al., 1998).

3.2.6. The Psychrometric Constant (γ)

The psychrometric constant is stated by the following formula:

$$\gamma = \frac{c_p \cdot P_{atm}}{\lambda_v \cdot \epsilon}. \tag{17}$$

P_{atm} is the atmospheric pressure (Pa) and ϵ is the ratio between the molecular weight water vapor and dry air, which is 0.622.

3.3. Water runoff rate

Darcy's Law (DL) is frequently favored for calculating water flow in peatlands due to its dependability and relatively straightforward approach to describing water movement through porous materials like peat. The assumption underlying DL is that water flows through the porous medium in a laminar manner, signifying that it travels in parallel layers without any interference between them. This is typically accurate for peatlands since the flow velocities are generally low enough to sustain laminar flow conditions.
Henry Darcy established DL in the 19th century, linking fluid flow through a porous medium to the pressure drop and the medium's permeability. The mathematical expression for DL is:

$$Q = \frac{\partial P}{\partial x} = \frac{-\kappa A}{\mu}\frac{\Delta P}{\Delta x} \Rightarrow Q_h = \frac{Q}{A} = \frac{\kappa}{\mu}\frac{\Delta P}{\Delta x} \tag{18}$$

where Q is volumetric flow rate (m^3/s), κ is permeability of the medium (m^2), μ is the dynamic viscosity ($Pa \cdot s$), which changes proportional to temperature. Due the measured temperatures fluctuating between 5^oC and 9^oC over the all periods μ proportionally fluctuates between $1.52 \cdot 10^{-3}$ and $1.34 \cdot 10^{-3}$, respectively (Paar, 2023). A is the cross-sectional area perpendicular to the direction of flow (m^2). With the uncertainty being too big in the depth of the aquifer, it is safer to assume that there is at least 1 m^3 at the top layer, hence setting $A = 1$ m^2. ΔP is the pressure drop throughout the medium (Pa) and Δx is the distance of the medium in the direction of flow (m).

In this study there is no accurate measure of the distance between the logging devices in the surface of the soil. They are all lowered with a metal wire at approximate depths. However, one centimeter of water is roughly equal to one hPa, hence the manually measured depths becomes imprtoant. Using Bernoulli's principle to prove this:

$$P_1 + \frac{1}{2}\rho v_1^2 + \rho g h_1 = P_2 + \frac{1}{2}\rho v_2^2 + \rho g h_2 \Rightarrow P_1 + \rho g h_1 = P_2 + \rho g h_2$$

$$\Rightarrow P_1 + \rho g \cdot 0 = P_2 + \rho g h_2 \Leftrightarrow P_1 - P_2 = \rho g h_2 \Leftrightarrow h_2 = \frac{\Delta P}{\rho g} \tag{19}$$

In this equation P is the pressure (Pa), ρ is the density of water (kg/m^3), v is the flow velocity (m/s), gravitational acceleration (9.82 m/s^2) and h is the height above a reference point (m). This proves that 1 cm

water $\approx 1\ hPa$. Because the flow of the water is particularly slow in a peatland it's safe to set $v = 0$, thus canceling out that term (Holden, 2005).

Applying this proof to Equation 18 and we get:

$$Q_h = \frac{\partial P}{\partial x} = \frac{-\kappa}{\mu}\frac{\Delta P}{\Delta x} = \frac{-\kappa \rho g}{\mu}\frac{\Delta z}{\Delta x} \tag{20}$$

A key component of DL is the permeability of the medium (κ), which accounts for the ease with which water can flow through the porous material. In peatlands, the permeability can vary significantly due to factors such as peat type, degree of decomposition, and water content. DL allows for this variability to be taken into account when calculating water flow. Additionally, μ also plays a role in the ease of the flow. Due to both permeability and viscosity of the water being the main drivers in how well the water flows through the soil, they are combined as the ratio between the two parameters; $k = \kappa/\mu$ and used to carry out the numerical calculations in this study. Because the peat moss not being uniformly distributed, the most accurate way of finding k through out the bog is to set the water balance equation as a function of k and in that way establish a value for k as it varies on where the measurements are taken:

$$\Delta h(k) = P_h - ET_h - Q_h = P_h - \left(\frac{\Delta(R_n - G) + \rho_a c_p(\delta_e)g_a}{(\Delta + \gamma(1 + g_a/g_s))L_v}\right) - \left(-k\rho g\frac{\Delta z}{\Delta x}\right) \tag{21}$$

3.4. The Chi-Squared technique

The chi-squared technique is a statistical method employed to assess the goodness of fit between observed data and an expected model, proving especially useful for categorical data. In the context of determining an appropriate k value for DL in a specific area, the chi-squared technique calculates the chi-squared statistic (χ^2), which represents the sum of the squared differences between observed values (O) and expected values (E) divided by the expected values:

$$\chi^2 = \sum_{i=1}^{n}\frac{(O_i - E_i)^2}{E_i} \tag{22}$$

Observed values refer to collected data, while expected values correspond to predictions made by a model. A lower chi-squared statistic indicates a better fit between the data and the model (Biswal, 2023).

Applying the chi-squared technique involves calculating the expected values for fluid flow through a porous medium for each k value being tested, based on a given model or theory. Subsequently, the chi-squared statistic for each k value is computed using the formula mentioned above. The degrees of freedom are determined by taking the total number of k values tested and subtracting one. A chi-squared distribution table is consulted to identify the critical chi-squared value corresponding to a chosen significance level and degrees of freedom. A calculated chi-squared statistic that is less than or equal to the critical value suggests that the observed and expected values do not significantly differ, indicating that the k value in question provides a good fit for the data.

A diagram displaying k values on the x-axis and the corresponding chi-squared statistic values on the y-axis can be plotted. The optimal k value corresponds to the lowest chi-squared statistic value on the graph, as this signifies a better fit between the observed data and the model employing that particular k value. An example of what a resulting plot of this technique can look like can be seen in Figure A17.

3.5. Uncertainty calculations

When conducting this research, the Monte Carlo method was used to estimate as close to real-life scenarios as possible, this meaning as close to the measured data as possible. The Monte Carlo method is a computational technique that involves running a large number of simulations with random inputs to estimate the outcome of a process or model. It's widely used in within physics and mathematics to solve problems that involve

uncertainty, complex systems, or probabilistic models.

In the context of the Monte Carlo method, standard deviation plays a significant role in quantifying the variability or dispersion of the simulation results.

When using the Monte Carlo method a first step is to define input distributions. Input variables are often represented as probability distributions that capture the uncertainty or variability of the inputs. The standard deviation is a key parameter of many probability distributions, such as the normal distribution, which is characterized by its mean and standard deviation. By specifying the standard deviation for each input variable, it is possible to define the range and spread of possible values that the variable can take.

In a Monte Carlo simulation, generated random samples are drawn from the input distributions for each variable. The standard deviation of the distribution influences the spread of the sampled values. A larger standard deviation will result in a wider range of sampled values, while a smaller standard deviation will produce a more concentrated range of values around the mean.

With the random samples for each input variable, the simulations are run, and the outputs are calculated. This process is repeated a large number of times, generating a distribution of output values that represents the possible outcomes of the model or process under study (Figure A18).

3.6. Interpolating the water flow

The Triangulated Irregular Network (TIN) interpolation is a geospatial analysis instrument in QGIS, utilized to produce a continuous surface from irregularly distributed points with known elevation values. It is mainly used for creating digital elevation models (DEM) and analyzing topographical or environmental data.

TIN interpolation forms a network of non-overlapping triangles using input points as vertices. It applies the Delaunay triangulation method to guarantee that no other points are within each triangle's circumscribed circle (Wikipedia, 2023). The elevation of a point within a triangle is calculated through linear interpolation based on the weighted average of elevations at the triangle vertices.

To estimate the resulting vector of groundwater flow, DL is used in conjunction with the generated DEM by examining each pixel and carrying out the following numerical calculations for each point. By calculating the vector ($\overrightarrow{V}$) between two points, find the magnitude ($||V||$) of the vector, then normalize the vector ($\overrightarrow{U}$), and finally sum them up in a resulting vector ($\overrightarrow{V_f}$):

$$
\begin{aligned}
\overrightarrow{V} &= (x_2 - x_1, y_2 - y_1, z_2 - z_1), \\
||V|| &= \sqrt{(x_2 - x_1)^2 + (y_2 - y_1)^2 + (z_2 - z_1)^2}, \\
\overrightarrow{U} &= \frac{V}{||V||}, \\
\overrightarrow{V_f} &= \sum_{i=1}^{n} \left(Q_i \cdot \overrightarrow{U_i} \right).
\end{aligned}
\tag{23}
$$

4. Results and Discussion

The on-site weather station employs an array of instruments to gather meteorological data; however, several of these instruments exhibit limitations. For instance, the humidity sensor is enclosed in a box (Figure A15), preventing it from accurately measuring external relative humidity (Stull, 2017). Additionally, airborne leaves, twigs and bird droppings occasionally clogs the funnel of the rain-measuring sensor. Consequently, precipitation data from SMHI's Hästveda weather station, located 23 km away, must be used. This discrepancy can particularly affect rain gauge readings, especially during intense local showers in summer. Rainfall measurement presents a significant challenge, even for well-established institutions like SMHI, due to factors such as wind forcing rain to steep angle of incidence (Jiang et al., 2020). Additionallyr, heavy showers can cause water to splash out of the collection cup, leading to big underestimations (Ciach, 2003).

In the absence of data or information regarding the stomatal and aerodynamic resistance values specific to Fäjemyren, FOA56 values was utilized. While a perfect correspondence cannot be expected due to the peatland's diverse flora, FAO56's consideration of short grass and well-watered conditions presents certain similarities that justify its application as provisional data. The resistances incorporated in the FAO56 equation account for energy exchange and moisture flux between the surface and the atmosphere, aspects that are also relevant to bog environments. Consequently, employing FAO56 resistances in the standard PME can yield a reasonably accurate estimation of ET for bogs, while recognizing potential deviations stemming from site-specific characteristics.

The on-site weather station lacks a wind-measuring instrument, necessitating the use of data from SMHI's Bjärnum station, situated 10 km away. Wind conditions varies significantly at a local level due to factors such as vegetation-induced friction and the formation of eddies in diverse landscapes (Donald Ahrens & Henson, 2015). However, across a cross-sectional distance of ± 20 km, wind conditions should be relatively consistent (DeGaetano, 1996), justifying the usage of data that may seem to be taken very far away.

Despite the potential for not fully precise data, conducting an experiment is still valuable from an experimental standpoint. Moreover, even approximate data can provide insights into underlying physical processes, which can then be refined through further experimentation and analysis.

While the SMHI data was complete, the on-site ReefNet logger data contained substantial gaps, some lasting up to a year. Although the weather station's water logger had tracked water table changes since 2015, it doesn't track water temperature, a crucial parameter for calculating ET. As a result, the combined data from the weather station and loggers was restricted to two summer and two winter periods, with climate conditions that, unfortunately, were quite similar. Both summer periods were characterized as hot than the average, with seasonal rain normal or slightly lower than the average. The winter periods were charactazied as mild and normal, with slightly more precipitation than usual.

- *Period 1* (P1): The summer of 2019 (SMHI, 2019)
- *Period 2* (P2): Winter 2020/2021 (SMHI, 2021)
- *Period 3* (P3): Summer 2022 (SMHI, 2022a)
- *Period 4* (P4): Winter 2021/2022 (SMHI, 2022b)

During periods P1 and P3, the measured data shows a consistent rise in water temperature, while the opposite trend is observed during P2 and P4, with temperatures exhibiting a steady decline. Due to observation, the value for viscosity μ is selected to be a constant mean, equal to $1.43 \cdot 10^{-3}$, which allows for a simplified representation of the varying temperature effects on viscosity when computing DL as a driver for the periods.

Regardless of the measured data having the interruptions, the loggers are known to exhibit drift (Section 2.2.) over a longer period of time (years), selecting shorter time periods is expected to minimize this issue. However, even within these shorter time intervals, the loggers exhibit considerable variation in their behavior. Given the current size of the study area, it is not very likely that the observed peaks in the data are attributable to localized precipitation events (Yuter & Houze Jr, 1995).
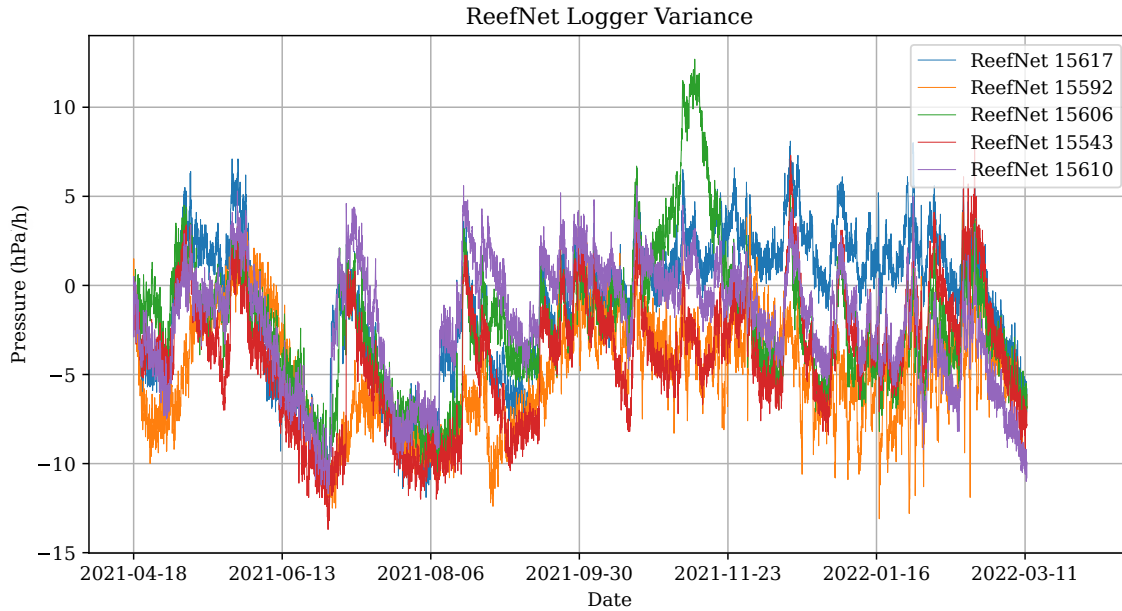
Figure 4: Data measured by the ReefNet loggers within the study area. By limiting the data plotted to the 1h based intervals and that which is continuous, the plot starts on the 4th of April, 2021. All the data are adjusted to start at zero, to get a better picture of how they vary.

The water table changes exhibit distinct individual behavior at each coordinate, as illustrated in Figure 4. It is evident that some loggers display individual peaks above and below the average, and there are instances where loggers intersect, with one suddenly indicating significantly higher pressure than another. Given this behaviour, it is important to point out that the runoff rate, calculated with DL, in real time scenarios indeed have small fluctuations, as the height difference between point 1 and point 2 most likely does not change in a similar fashion. The fluctuations are not significant, due to the small height difference, compared to the dinstance between then, still they should not be forgotten.

Given this variability, it is not crucial to focus on each logger's data; rather, highlighting the fact that the water is not uniformly represented in the bog suffices. Consequently, three representative loggers are featured in the diagrams: the northernmost logger (ReefNet 15562, later replaced by HOBO 20796674 in 2022), the central logger (ReefNet 15606), and the southernmost logger (ReefNet 15610).

4.1. Period 1 - May-Aug, 2019

A critical challenge encountered during the development of the model pertains to the configuration of the ReefNet loggers. For P1, all instruments, except for 15610, were programmed to record data every 12 hours. In contrast, logger 15610 was set to log data hourly. While the water not being uniformly distributed across the bog remains a fact, it can prove in this one case, displayed in Figure 5, that the logger tracks measurements quite differently when being set to log on an hourly basis. 15562 and 15606 both shows a steady increasing trend during the whole period and after around the 5th of May never showing a negative result of the pressure, contrary to 15610 which shows an entirely different trend.
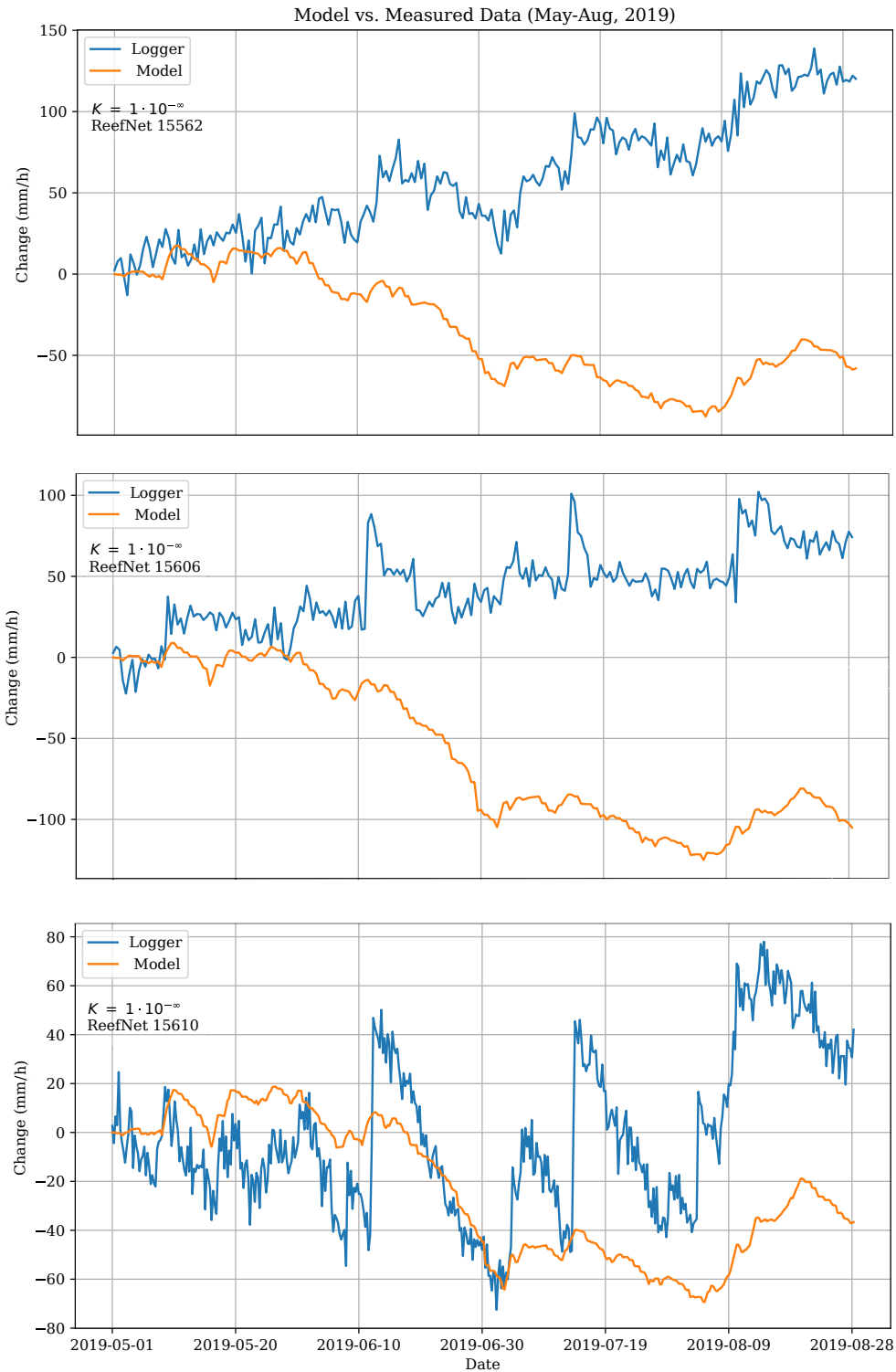
Figure 5: Examples of the data measured by the loggers compared to the created model on *Period* 1; 1st of May, 2019 to 28th of August, 2019. The loggers ReefNet 15592 and 15543 has a 12h logging interval, while the ReefNet logger 15610 conducts hourly logging.

Even if the model shows to be a slightly better fit for 15610 in this period, it still generates $k = 1 \cdot 10^{-\infty}$. The issue originates in the ET being estimated to be a lot higher from around the 6th of June, a point where the precipitation never comes up to the same levels as ET. With this estimation, the runoff would virtually be zero, as can be seen in Figure 6, something that is highly unlikely.

To accurately estimate ET on both daily and seasonal scales, it is essential that instruments record data at an as high diurnal resolution as possible, preferably down to 1 hour intervals (Lundquist & Cayan, 2002). This necessity is demonstrated in Figure 5. The 12-hour logging intervals of the other loggers are inconsistent, with some recording at 3:00 and 15:00, while others log at 4:00 and 16:00. None of the selected diurnal timestamps for logging are guaranteed to capture the positive or negative peaks in the data essential for estimating ET. When writing the model, this data proved to be not at all useful as can be seen in Figure 6, where the runoff driver is zero everywhere.
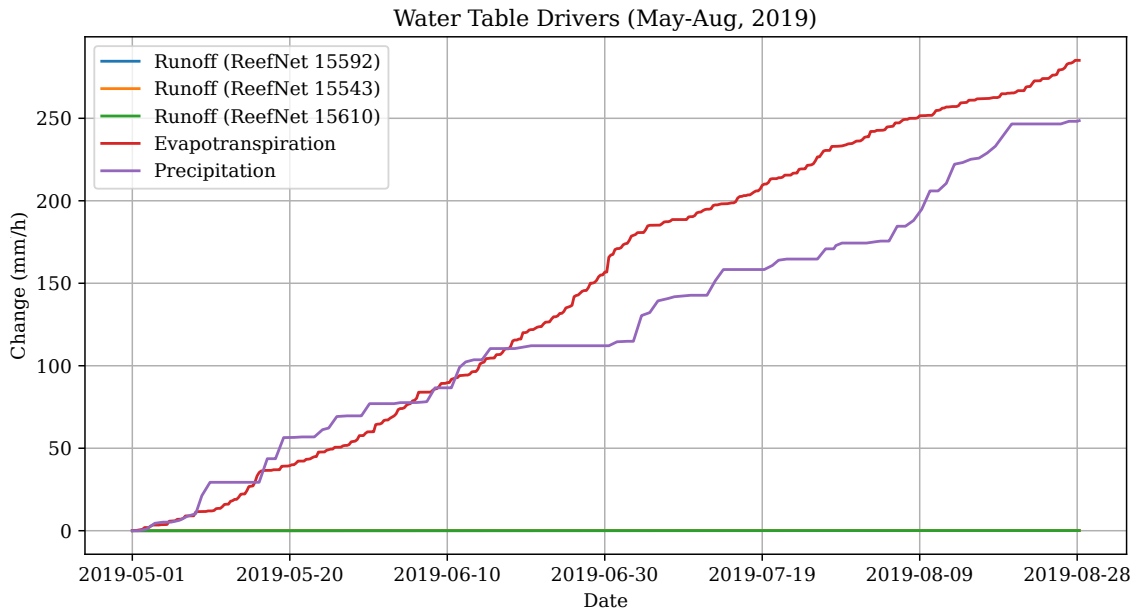

Figure 6: Plot showing the main drivers of *Period* 1. Run off is zero at every point.

4.2. Period 2 - Nov-Feb, 2021/2022

This period shows very interesting results. Analyzing Figure 7 the deviations are still pronounced, but the model follows the curvature rather smooth in both the 15562 and the 15610 case. The peaks could be due to the precipitation data not completely reflecting the precipitation to that of Fäjemyren. 15606 shows a huge deviation during December. This increase of the water table could potentially show the water flowing greatly temporarily in this direction, as it normalizes in January where the deviation is not as pronounced anymore, when comparing it to the other two cases. Even though there are large deviations it still, in comparison to P1, shows an a lot better fit. Snow may also be a reason for the peaks. With the snow being registered as precipitation at SMHI's weather station, the loggers in the bog wouldn't register the change in the water table until it thaws. With the area of study being situated in Scania, there are no longer periods of snow cover, whereas when the precipitation is snow, it has most likely thawed within two weeks. Moreover, the model produced values for the permeability as well, which are all in range of the soil in a peatland (Price, 2003).
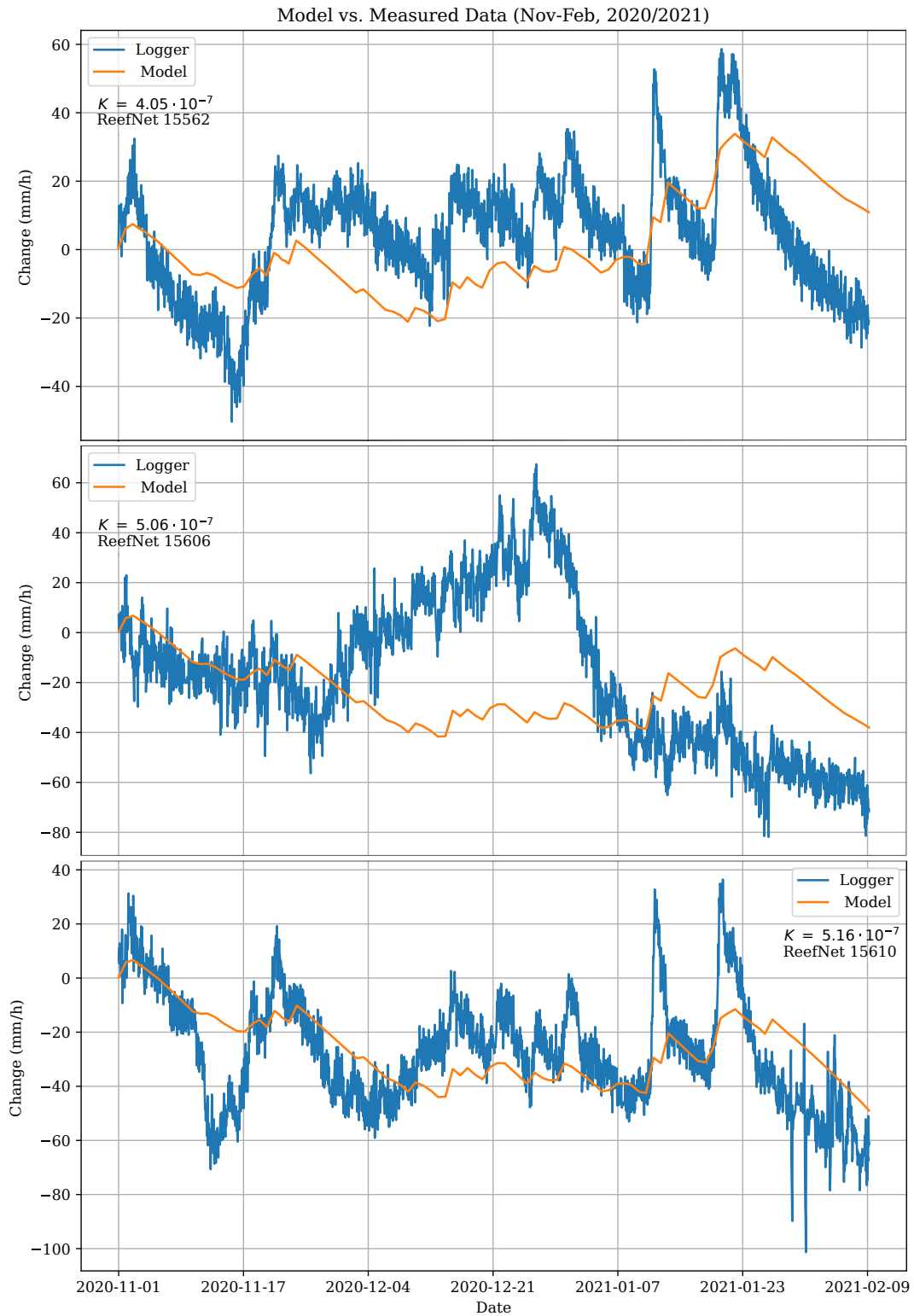
Figure 7: Examples of the data measured by the loggers compared to the created model on *Period* 2; 1st of November, 2020 to 9th of February, 2021.

The figures generated for this winter seasons (Figure 7, 8) indicate that ET is virtually negligible. During sub-zero periods, when soil freezing occurs, this observation holds true (Lafleur et al., 2001), and as temperatures approach zero, ET substantially decreases.

With an assumption is that ET constitutes 2/3 of the precipitation (Waddington & Roulet, 2000), it is crucial to acknowledge that this is an annual estimation, implying that the majority of ET takes place during the summer half of the year. Additionally the months with the lowest ET output is typically November, through February (Brutsaert, 2005). This discontinuation is simulated and visualized in Figure A18. Consequently, the water runoff rate becomes the primary negative driver (Figure 8) during winter months (Woo & Young, 2006). As the nature of viscosity changes proportional to temperature, a natural change in the runoff drivers would show a slight curvature instead of a linear increase. Worth pointing out is the lack of small fluctuations in the runoff drivers as well, which is mentioned earlier.

Morever, the period shows an over all decline in the water table which can be seen in both Figure 7 and 8. In the latter mentioned figure, it can be seen since the runoff rate exceeds the precipitation in two of the cases.
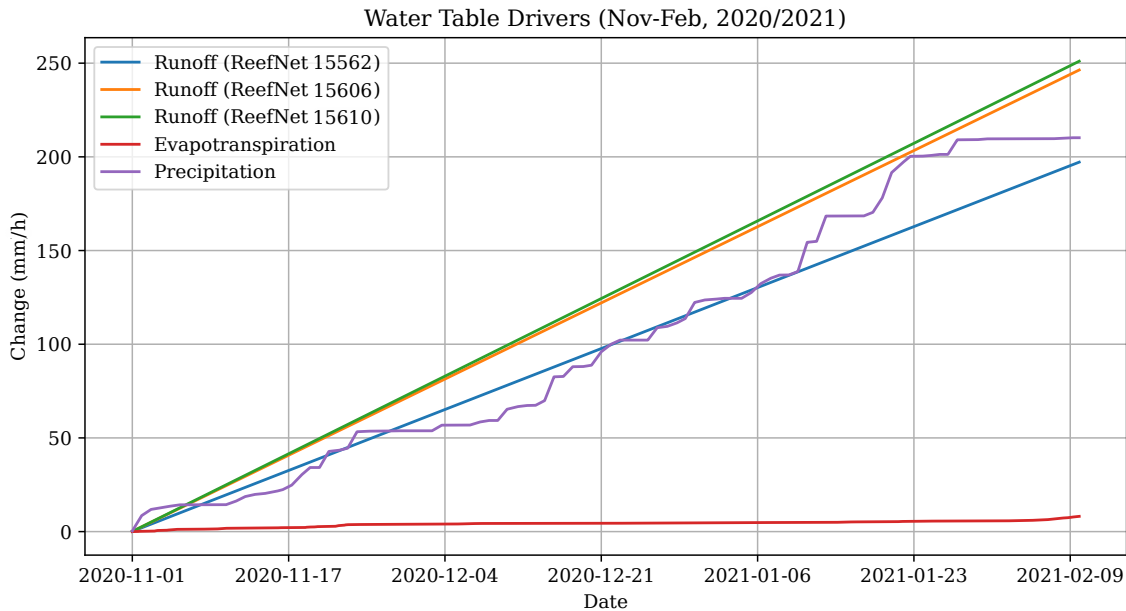

Figure 8: Plot showing the main drivers of *Period* 1. Evapotranspiration low due to annual low temperatures and low amounts of solar radiation.

4.3.   Period 3 - May-Aug, 2022

The following period shows the best results. Displayed in Figure 9, the model shows an almost perfect curvature fit to the measured data. Similar to P2, there are peaks which occur for natural reasons. As mentioned in section 4.2., these positive devations are most likely showing do to the precipitation not reflecting that of which is taking place at Fäjemyren.
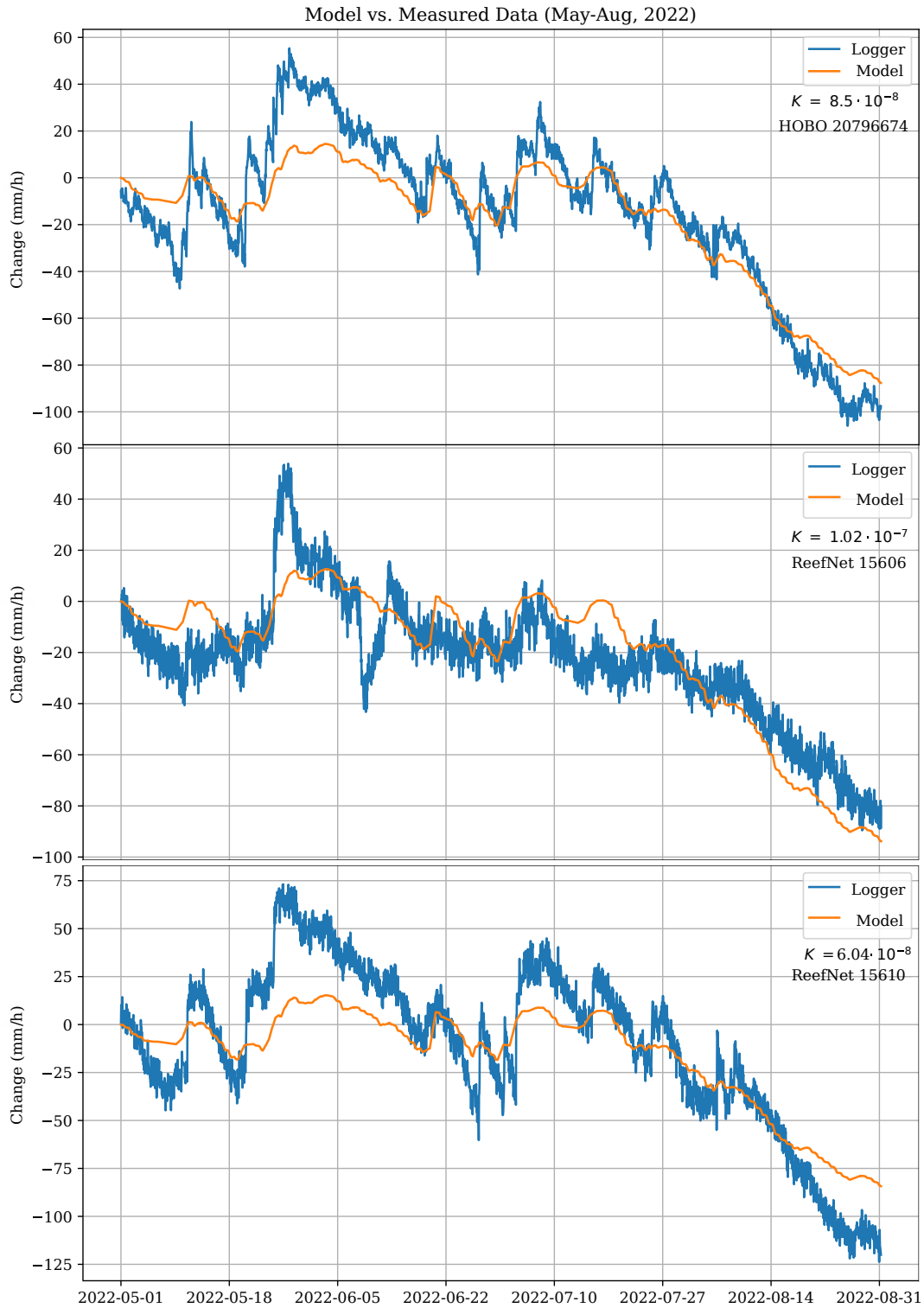
Figure 9: Examples of the data measured by the loggers compared to the created model on *Period* 3; 1st of May, 2022 to 31st of August, 2022.
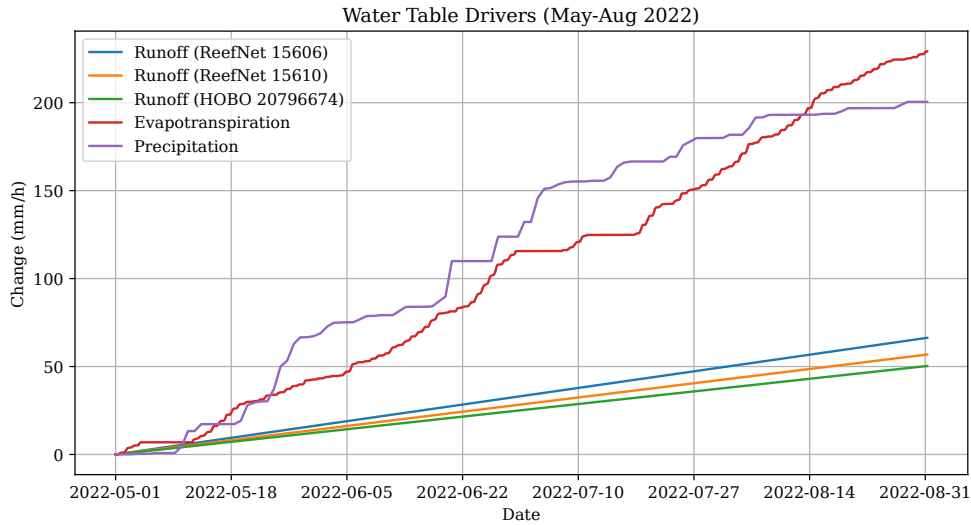
Figure 10: Plot showing the main drivers of *Period* 3. The run off being the smaller driver, as the annual high temperatures give rise to an increasing evapotranspiration rate.

Although discussing in section 4.1. that the model appears to yield higher ET values than anticipated, it is important to note that during periods of above-average heat exposure, ET can indeed surpass the precipitation levels (Roderick & Farquhar, 2002). Both the summers of 2019 and 2022 were characterized by higher temperatures and lower precipitation compared to average years (SMHI, 2019)(SMHI, 2022a), suggesting that the model's output may not deviate as significantly as initially presumed. This could indicate that there would be an error in the data management of P1. Figure 10 represents a case of what one could expect the water balance equation would represent during a hot summer event in Scania, with all drivers being present and ET being the most pronounced due to high rates of solar radiation.

4.4.   Period 4 - Nov-Feb, 2022/2023

Despite the assertion from the SMHI that the two winter periods exhibit similarities, a close examination reveals distinct differences between them. This discrepancy may be attributed to the study's focus on a localized region. In contrast to the information presented in Figure 8, Figure 12 displays a precipitation total that is 50 mm greater, with the runoff rate exhibiting an almost inverse proportionality. Consequently, there is an overall increase in the water table during this period (Figure 11).

It is crucial to acknowledge that snow may influence the precision of the developed model, resulting in deviations between the model's estimations and the actual observed data. Thus, when interpreting these findings, it is essential to carefully consider the impact of snow on the water table dynamics.
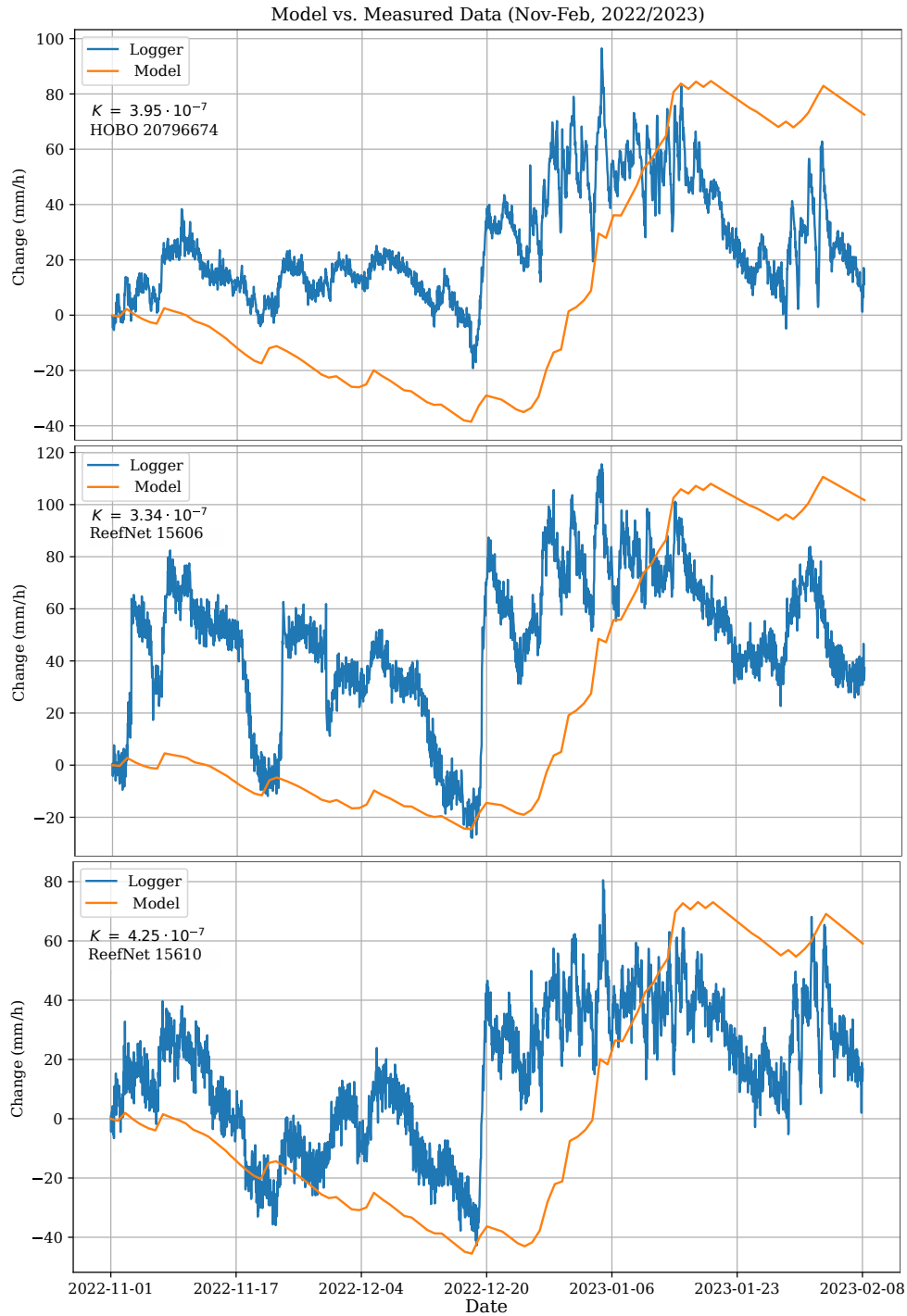
Figure 11: Examples of the data measured by the loggers compared to the created model on *Period* 4; 1st of November, 2022 to 9th of February, 2023.

These observations suggests that non-uniform water flow is the primary cause of these discrepancies. Although precipitation data collected at the SMHI Bjärnum station does not perfectly represent the conditions within the bog, the observed differences between the station's data and the bog conditions, as illustrated

in Figure 7 (ReefNet 15606) and Figure 4 and Period 4 (Figure 11), should not be as pronounced as they appear. This could indicate a scenario where the surrounding clay or sediment has been breached, causing the bog to transition into a fen due to erosion (Limpens, Berendse, Blodau, Canadell, et al., 2008). Partial erosion of the clay or sediment layer could lead to increased water flow from outside, during periods of high precipitation, resulting in a rise in the availability of the sparse nutrients within the bog (Siegel & Glaser, 1987a). This process could also contribute to the encroachment of vegetation observed in the area (Reeve et al., 2001)(Figure A16).
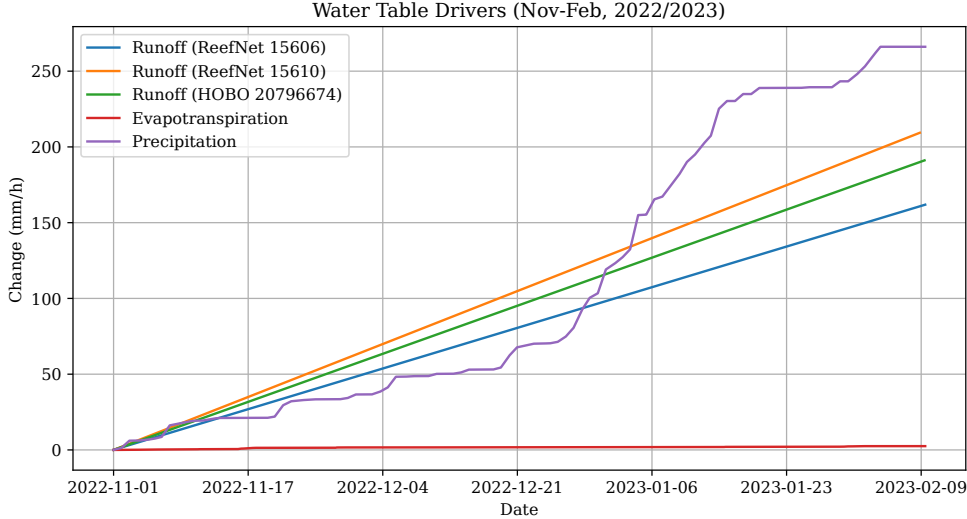

Figure 12: Plot showing the main drivers of *Period* 4. Again, runoff is the primary driver having a negative impact on the change in the water table.

From the perspective of creating a model like this, acquiring a full year's worth of data would be invaluable. This would necessitate refining the model to account for the fact that the dynamic viscosity μ cannot be treated as a constant but must be considered a temperature-dependent parameter. Nonetheless, incorporating such data would provide a more comprehensive evaluation of the model's performance.

4.5. Additional Remarks

When utilizing the Monte Carlo model for estimating the driving factors, it was demonstrated that the uncertainty in the GPS measurements had a negligible impact on the flow rate. With an uncertainty of merely $\pm 1.3 \ cm$, the resulting variation in flow rate calculation over distances spanning tens of meters was determined to be less than $1 \cdot 10^{-15} \ m^3/s$. Without any reported uncertainties in the precipitation from SMHI, applying the Monte Carlo model is not feasible. Consequently, this method was only utilized in the ET calculations.

To achieve the most accurate estimation of the k value, the model is executed utilizing all available logger data. Table 1 displays the k value for each coordinate, along with a mean value that serves as the primary k value for the respective period. The k value exhibit fluctuations between $4.31 \cdot 10^{-7}$ and $7.40 \cdot 10^{-7}$, resulting in a well-defined permeability within a peatland region (Price, 2003). It is roughly $3 \cdot 10^{-7}$ smaller during the summer period compared to the winter period, which coincide with what is represented in the sections concerning each period.

It is worth noting that, owing to P1 consistently yielding a value of $1 \cdot 10^{-\infty}$, the first column exclusively

comprises zeros. This observation is crucial for understanding the implications of the hydraulic conductivity data.

ID	Period 1	Period 2	Period 3	Period 4
ReefNet 15562 / HOBO 20796674	0	$4.05 \cdot 10^{-7}$	$8.50 \cdot 10^{-8}$	$3.95 \cdot 10^{-7}$
ReefNet 15617	0	$4.06 \cdot 10^{-7}$	$9.60 \cdot 10^{-8}$	$4.25 \cdot 10^{-7}$
ReefNet 15592	0	$5.06 \cdot 10^{-7}$	$1.12 \cdot 10^{-7}$	$4.15 \cdot 10^{-7}$
ReefNet 15606	0	$4.16 \cdot 10^{-7}$	$1.02 \cdot 10^{-7}$	$3.34 \cdot 10^{-7}$
ReefNet 15543	0	$4.55 \cdot 10^{-7}$	$1.11 \cdot 10^{-8}$	$4.75 \cdot 10^{-7}$
ReefNet 15616 / HOBO 20796679	0	$4.8 \cdot 10^{-7}$	$5.15 \cdot 10^{-8}$	$3.54 \cdot 10^{-7}$
ReefNet 15610	0	$5.36 \cdot 10^{-7}$	$6.04 \cdot 10^{-8}$	$6.17 \cdot 10^{-7}$
Mean k	**0**	**$4.58 \cdot 10^{-7}$**	**$7.40 \cdot 10^{-7}$**	**$4.31 \cdot 10^{-7}$**

Table 1: The estimated permeability for each logger coordinate during the four periods. The HOBO loggers were not deployed until period 3.

Given the implications of non-uniformity within the bog, the utilization of manually collected measurements becomes crucial. The overall estimated value for the k suggests that the soil exhibits fibric peat characteristics. Fibric peat, characterized by its less decomposed nature, typically exhibits a permeability ($\kappa = \mu/k$) range of 10^{-3} to 10^{-5} m/s. This is in contrast to moderately decomposed (hemic peat) and less decomposed (sapric peat), which display permeability ranges of 10^{-5} to 10^{-7} m/s and , 10^{-7} to 10^{-9} m/s respectively (Price, 2003).

By utilizing DL, and incorporating the mean k value estimated for the P4 ($4.31 \cdot 10^{-7}$) (Table 1), it becomes interesting to facilitate an examination of water flow dynamics within the peatland. By utilizing the manual measurements, conducted with the Spear, it is possible to import the data into GIS-programs (Geographical Information Science) to examine further, by computational interpolation. Using TIN-interpolation and Delaunay triangulation in QGIS, it is possible to interpolate areas as depicted in Figure 13. The figure shows an interpolation of how the height differs as one moves from the center towards the outskirts. The results do not significantly deviate from what is expected for a bog like Fäjemyren, where the elevation is higher at the center (Siegel & Glaser, 1987b), particularly in a relatively small area like the the study area.
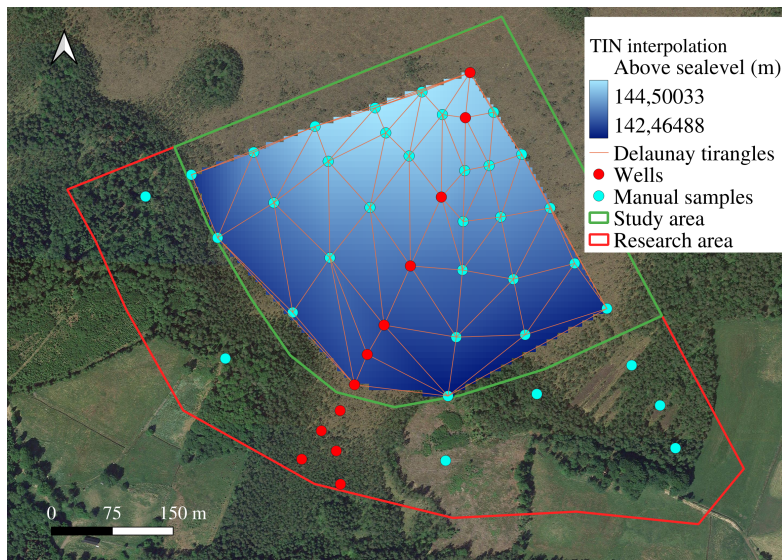

Figure 13: A TIN-interpolation of the study area.

A denser grid of measurement points yields more accurate results when determining the water flow characteristics, which could prove useful in terms of finding a potential second positive driver to the water balance equation (Equation 4). Furthermore, manual data collection is both time-consuming and labor-intensive, which justifies the employment of GIS interpolation tools. The potential flow of water in the bog can be determined by initially applying the DL to each pixel and its adjacent neighboring pixels in the generated DEM. By applying the eight caclulated scalar products, for each pixel, the resultant vectors can be computed using Equation 23. This calculation yields the vector field illustrated in Figure 14.
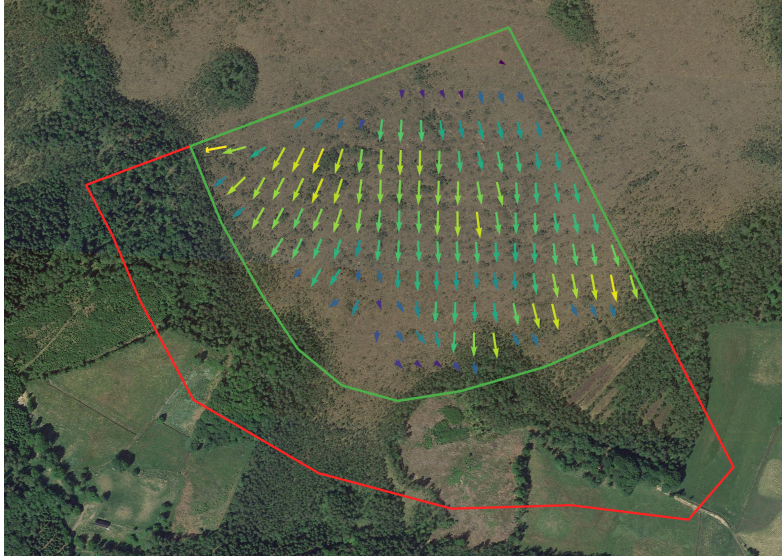

Figure 14: A is a vector field, showing the possible flow in this part of Fäjemyren.

The outermost points, lacking eight neighboring points, may not accurately represent the correct magnitude or direction of the vector. Nevertheless, the inner field, despite being a product of GIS interpolation, exhibits intriguing patterns.

In summary, a particularly noteworthy aspect of this study is the excellent model fit observed during P4. This demonstrates not only the model's possible ability to accurately capture changes in the water table, when utilizing accurate data (Figure 9) but also its effectiveness in representing the distribution of the various drivers (Figure 10). This performance highlights the model's potential for application in similar scenarios.

5. Conclusion

The research project investigates vegetation encroachment in the Fäjemyren bog, located in northern Scania, Sweden, as part of an ongoing initiative at INES (Lund University), co-led by Veiko Lehsten. It examines the impact of climate change-induced drought periods on tree seedling root systems. This study is a branch of the larger research project, which focuses on modeling groundwater table response to rainfall, exploring rainwater absorption, water flow rate, and the contribution of evapotranspiration to hydrological processes. A model replicating water table fluctuations is constructed using meteorological data.

Data collection for this research requires fieldwork. A typical field day consists approximately four hours of measurements and readings, depending on weather conditions. The challenging terrain necessitates intermittent rest periods. Various scientific instruments are used to monitor changes in soil pressure, water table height and temperature. A handmade "Spear" measures subsurface water levels, while a water probe detects surface levels. Water level loggers continuously monitor water levels, and an on-site weather station collects meteorological data. Additional atmospheric information is sourced from the Swedish Meteorological and

Hydrological Institute's database.

Data from different instruments are consolidated and analyzed using Python and modules for organization, processing, and visualization. QGIS software aids in map examination and area interpolation. The central theory relies on the water balance equation ($\Delta h = P_h - ET_h - Q_h$), with precipitation, evapotranspiration, and water runoff as primary determinants. The water flow coefficient k is essential for calculating the runoff rate; however, due to the non-uniform soil properties of peatlands, it cannot be considered static and requires estimation. The water balance equation, expressed as a function of k, serves as the foundation for creating the model.

The k value, which is the ratio of permeability of the soil and the viscosity of the water, is determined using the chi-squared method, which assesses the goodness of fit between observed data and an expected model. This involves calculating expected values, comparing them to observed values, and consulting a chi-squared distribution table for the optimal fit. The Monte Carlo method, a computational approach using random inputs for numerous simulations, estimates process or model outcomes. This method addresses uncertainty and complex systems and is widely used in physics and mathematics. Standard deviation quantifies variability, and input variables in Monte Carlo simulations are represented as probability distributions with specific standard deviations. The approach is selected to evaluate evapotranspiration.

Due to the complex integration of the Penman-Monteith equation and Darcy's Law, the study focuses on a smaller area than originally anticipated for calculations. This decision was influenced by the unavailability of stomata parameters for various forest plants and intersecting non-peat soil permeability measurements. Using Lantmäteriet's data layers and comparing soil type layers with satellite imagery allowed for accurate estimations of tree encroachment and soil transitions, justifying the study area emphasis.

The results highlight limitations in the on-site weather station, including inaccurate humidity measurements and occasional rain sensor clogging. Consequently, precipitation data from a nearby station is used, potentially impacting local shower readings. Additionally, the lack of wind-measuring instruments necessitates using data from a station 23 km away. Local turbulence and eddies are disregarded, and the wind conditions are assumed to be consistent at this distance.

The findings reveal significant data gaps, necessitating the limitation of the study to two summer and two winter periods with comparable climatic conditions. Configuration issues with loggers, recording data at irregular intervals, compromised the accuracy of evapotranspiration estimation. In the absence of data on stomatal and aerodynamic resistance values specific to the study site, FAO56 Penman-Monteith equation values were used. Although not perfect, these values provide a reasonably accurate estimation of evapotranspiration for bogs.

The model generated high evapotranspiration rates during the summers, which was expected during periods of above-average heat exposure. During these periods evapotranspiration rates surpass precipitation levels. The winter season demonstrated that evapotranspiration is virtually negligible, with the water runoff rate being the primary negative driver during those months. Considering the bog's non-uniformity, manual measurements are crucial for discerning soil properties. Permeability estimation indicates the presence of fibric peat, and Darcy's Law facilitates the analysis of water flow dynamics. While labor-intensive, GIS interpolation tools offer a valuable alternative for data collection and interpretation, ultimately contributing to a better understanding of the complexities of peatland ecosystems.

8. References

Allen, R. G., Raes, D., & Smith, M. (1998). Fao penman-monteith equation. In L. S. Pereira (Ed.), *Crop evapotranspiration - guidelines for computing crop water requirements*. FAO - Food; Agriculture Organization of the United Nations.

Bailey, S. C. C., Vallikivi, M., Hultmark, M., & Smits, A. J. (2014). Estimating the value of von kármán's constant in turbulent pipe flow. *Journal of Fluid Mechanics*, *749*, 79–98. https://doi.org/10.1017/jfm.2014.208

Baldocchi, D. (2014). Espm 129 [Accessed: 22th April, 2023]. https://nature.berkeley.edu/biometlab/espm129/overheads/Lecture_15_ESPM_129_Humdity_part_2_Overheads_2014.pdf

Berglund, K. (2000). Torvmarken, en resurs i jordbruket igår, idag och även i morgon. *Svensk mosskultur: odling, torvanvändning och landskapets förändring*, *2000*, 483–498.

Biswal, A. (2023). What is a chi-square test? formula, examples application [Accessed: 2023-05-10.]. https://www.simplilearn.com/tutorials/statistics-tutorial/chi-square-test

Brutsaert, W. (2005). Hydrology: An introduction cambridge university press. *New York*.

Childs, P. (2001). *Practical temperature measurement*. Elsevier.

Ciach, G. J. (2003). Local random errors in tipping-bucket rain gauge measurements. *Journal of Atmospheric and Oceanic Technology*, *20*(5), 752–759.

DeGaetano, A. T. (1996). Recent trends in maximum and minimum temperature threshold exceedences in the northeastern united states. *Journal of Climate*, *9*(7), 1646–1660.

Dingman, S. L. (2015). *Physical hydrology*. Waveland press.

Donald Ahrens, C., & Henson, R. (2015). Meteorology today: An introduction to weather, climate and the environment.

Engineering-ToolBox. (2003). Air - density, specific weight and thermal expansion coefficient vs. temperature and pressure [Accessed: 2023-05-08.]. https://www.engineeringtoolbox.com/air-density-specific-weight-d_600.html

Engineering-ToolBox. (2004). Air - specific heat vs. temperature at constant pressure [Accessed: 2023-04-17.]. https://www.engineeringtoolbox.com/air-specific-heat-capacity-d_705.html

Engineering-ToolBox. (2010). Water - heat of vaporization vs. temperature [Accessed: 2023-04-22.]. https://www.engineeringtoolbox.com/water-properties-d_1573.html

Fath, B. D. (2018). *Encyclopedia of ecology*. Elsevier.

Graf, A., van de Boer, A., Moene, A., & Vereecken, H. (2014). Intercomparison of methods for the simultaneous estimation of zero-plane displacement and aerodynamic roughness length from single-level eddy-covariance data. *Boundary-Layer Meteorology*, *151*(2), 373–387. https://doi.org/10.1007/s10546-013-9905-z

Henderson-Sellers, B. (1984). A new formula for latent heat of vaporization of water as a function of temperature. *Quarterly Journal of the Royal Meteorological Society*, *110*(466), 1186–1190. https://doi.org/https://doi.org/10.1002/qj.49711046626

Holden, J. (2005). Peatland hydrology and carbon release: Why small-scale process matters. *Philosophical Transactions of the Royal Society A: Mathematical, Physical and Engineering Sciences*, *363*(1837), 2891–2913.

Jiang, G., Liu, J., Li, X., Liu, H., & Liao, A. (2020). Evaluation of measurement errors of tipping bucket rain gauges. *EGU General Assembly Conference Abstracts*, 6509.

Kaplan, E. D., & Hegarty, C. (2017). *Understanding gps/gnss: Principles and applications*. Artech house.

Kipp&Zonen. (2015). The working principle of a thermopile pyranometer [Accessed: 23/4 - 2023]. https://www.kippzonen.com/News/572/The-Working-Principle-of-a-Thermopile-Pyranometer

Klip&Zonen. (2015). *Cnr 4 net radiometer instruction manual* (v2104) [Available at https://www.kippzonen.com/Download/354/Manual-CNR-4-Net-Radiometer-English-V2104]. Klip & Zonen. The Netherlands.

Kujala, K., Seppälä, M., & Holappa, T. (2008). Physical properties of peat and palsa formation. *Cold Regions Science and Technology*, *52*(3), 408–414. https://doi.org/https://doi.org/10.1016/j.coldregions.2007.08.002

Lafleur, P., Roulet, N., & Admiral, S. (2001). Annual cycle of co2 exchange at a bog peatland. *Journal of Geophysical Research: Atmospheres*, *106*(D3), 3071–3081.

Limpens, J., Berendse, F., Blodau, C., Canadell, J. G., Freeman, C., Holden, J., Roulet, N., Rydin, H., & Schaepman-Strub, G. (2008). Peatlands and the carbon cycle: From local processes to global implications – a synthesis. *Biogeosciences*, *5*(5), 1475–1491. https://doi.org/10.5194/bg-5-1475-2008

Limpens, J., Berendse, F., Blodau, C., Canadell, J., Freeman, C., Holden, J., Roulet, N., Rydin, H., & Schaepman-Strub, G. (2008). Peatlands and the carbon cycle: From local processes to global implications– a synthesis. *Biogeosciences*, *5*(5), 1475–1491.

Lindsey, D. H., & Rebecca. (2022). Hasn't earth warmed and cooled naturally throughout history? [Accessed: 2023-02-08.]. https://www.climate.gov/news-features/climate-qa/hasnt-earth-warmed-and-cooled-naturally-throughout-history

Lowe, P. R., & Ficke, J. M. (1974). *The computation of saturation vapor pressure* (tech. rep.). NAVAL ENVIRONMENTAL PREDICTION RESEARCH FACILITY MONTEREY CA.

Lundquist, J. D., & Cayan, D. R. (2002). Seasonal and spatial patterns in diurnal cycles in streamflow in the western united states. *Journal of Hydrometeorology*, *3*(5), 591–603.

Monteith, J. L. (1965). *Evaporation and environment.*

Moore Jr., P. A., & Miller, D. M. (1994). Decreasing phosphorus solubility in poultry litter with aluminum, calcium, and iron amendments. *Journal of Environmental Quality*, *23*(2), 325–330. https://doi.org/https://doi.org/10.2134/jeq1994.00472425002300020016x

Murray, F. W. (1967). On the computation of saturation vapor pressure. *Journal of Applied Meteorology*, *6*(1), 203–204. https://doi.org/10.1175/1520-0450(1967)006<0203:otcosv>2.0.co;2

Paar, A. (2023). Viscosity of water [Accessed: 2023-05-08.]. https://wiki.anton-paar.com/se-en/water/

Peat formation [Accessed: 2023-02-07.]. (2019). https://peatlands.org/peat/peat-formation/

Pereira, L. S., Allen, R. G., Smith, M., & Raes, D. (2015). Crop evapotranspiration estimation with fao56: Past and future [Agricultural Water Management: Priorities and Challenges]. *Agricultural Water Management*, *147*, 4–20. https://doi.org/https://doi.org/10.1016/j.agwat.2014.07.031

Pls 15-20 [Rev. 3]. (2013). ELWATeknik.

Price, J. S. (2003). Role and character of seasonal peat soil deformation on the hydrology of undisturbed and cutover peatlands. *Water Resources Research*, *39*(9).

ProcessParameters. (2023). Pt100 sensor working principle [Accessed: 2023-04-23.]. https://www.processparameters.co.uk/pt100-sensor-working-principle/

Reeve, A., Siegel, D., & Glaser, P. (2001). Simulating dispersive mixing in large peatlands. *Journal of Hydrology*, *242*(1-2), 103–114.

Roderick, M. L., & Farquhar, G. D. (2002). The cause of decreased pan evaporation over the past 50 years. *science*, *298*(5597), 1410–1411.

Schaeffer, M., Eickhout, B., Hoogwijk, M., Strengers, B., Vuuren, Leemans, R., & Opsteegh, T. (2006). Co2 and albedo climate impacts of extratropical carbon and biomass plantations. *Global Biogeochemical Cycles 20 (2006) 2*, *20*. https://doi.org/10.1029/2005GB002581

Sensus ultra [Rev. 3]. (2018). ReefNet Inc.

Siegel, D. I., & Glaser, P. H. (1987a). Groundwater flow in a bog-fen complex, lost river peatland, northern minnesota. *The Journal of Ecology*, 743–754.

Siegel, D. I., & Glaser, P. H. (1987b). Groundwater flow in a bog-fen complex, lost river peatland, northern minnesota. *The Journal of Ecology*, 743–754.

Sjörs, H. (1959). Bogs and fens in the hudson bay lowlands. *Arctic*, *12*(1), 2–19.

SMHI. (2019). Summer of 2019 [Accessed: 2023-05-08.]. https://www.smhi.se/klimat/klimatet-da-och-nu/arets-vader/sommaren-2019-varmare-an-normalt-1.150462

SMHI. (2021). Winter of 2020/2021 [Accessed: 2023-05-08.]. https://www.smhi.se/klimat/klimatet-da-och-nu/arets-vader/vintern-2021-mycket-mild-inledning-1.167661

SMHI. (2022a). Summer of 2022 [Accessed: 2023-05-08.]. https://www.smhi.se/klimat/klimatet-da-och-nu/arets-vader/sommaren-2022-mycket-varm-i-ostra-gotaland-och-ostra-svealand-1.185036

SMHI. (2022b). Weather of 20212022 [Accessed: 2023-05-08.]. https://www.smhi.se/klimat/klimatet-da-och-nu/arets-vader/vintern-2022-forhallandevis-normal-1.179621

SMHI. (2023). Väder väderprognoser klimat- amp; vädertjänster i sverigenbsp; https://www.smhi.se/

Staib, R. (2015). Piezoresistive pressure sensors. https://www.avnet.com/wps/portal/abacus/solutions/technologies/sensors/pressure-sensors/core-technologies/piezoresistive-strain-gauge/

Stull, R. (2017). *Meteorology for scientists and engineers* (3rd Edition).

Technologies, P. P. S. (2011). *Rotronic mp102h instruction manual* (E-M-HM-V1$_1$2) [Available at https://www.processsensing.com/docs/manual/productattachments_files_e_-_e-m-hm-v1_12.pdf]. PST Process Sensing Technologies.

Topcon. (2016). *Topcon hiper hr* (Rev A) [Available at https://businesshub.topcon.com/medias/HiPer-HR-wners-Manual.pdf?context=bWFzdGVyfHJvb3R8MzUxMjg4N3xhcHBsaWNhdGlvbi9wZGZ8aDNhL2g2ZS84ODA0 Topcon.

U20 water level [Rev. 3]. (2018). HOBO.

Urieli, I. (1984). Specific heat capacities of air [Accessed: 2023-04-17.]. https://www.ohio.edu/mechanical/thermo/property_tables/air/air_Cp_Cv.html

Vaisala. (2021). *Vaisala ptb210 instruction manual* (B210942EN-E) [Available at https://docs.vaisala.com/v/u/B210942EN-E/en-US]. Vaisala.

Verhoeven, J. T. A., Maltby, E., & Schmitz, M. B. (1990). Nitrogen and phosphorus mineralization in fens and bogs. *Journal of Ecology*, *78*(3), 713–726. Retrieved February 8, 2023, from http://www.jstor.org/stable/2260894

Waddington, J., & Roulet, N. (2000). Carbon balance of a boreal patterned peatland. *Global Change Biology*, *6*(1), 87–97.

Wikipedia. (2023). Delaunay triangulation — Wikipedia, the free encyclopedia [[Online; accessed 07-May-2023]].

Woo, M.-k., & Young, K. L. (2006). High arctic wetlands: Their occurrence, hydrological characteristics and sustainability. *Journal of Hydrology*, *320*(3-4), 432–450.

Yuter, S. E., & Houze Jr, R. A. (1995). Three-dimensional kinematic and microphysical evolution of florida cumulonimbus. part i: Spatial distribution of updrafts, downdrafts, and precipitation. *Monthly Weather Review*, *123*(7), 1921–1940.

Appendix

Figure A1: Scotch Heather

Figure A2: Crossleaf Heather

Figure A3: Sheathed Cottonsedge

Figure A4: Example one of the age of a tree, with ruler

Figure A5: Example two of the age of a tree, with ruler

Figure A6: Average Birch height, average height person as reference

Figure A7: Average Scotts Pine height, average height person as reference

Figure A8: Showing the sponge characteristics of the soil

Figure A9: To the left: The Spear. To the right: ELWA PLS 15.

Figure A10: Taking manual measurements with the "Spear"

Figure A11: Example of a well where the loggers are located

Figure A12: Reading out a water logger (HOBO)

Figure A13: Measuring the height of the water in a well with a ruler

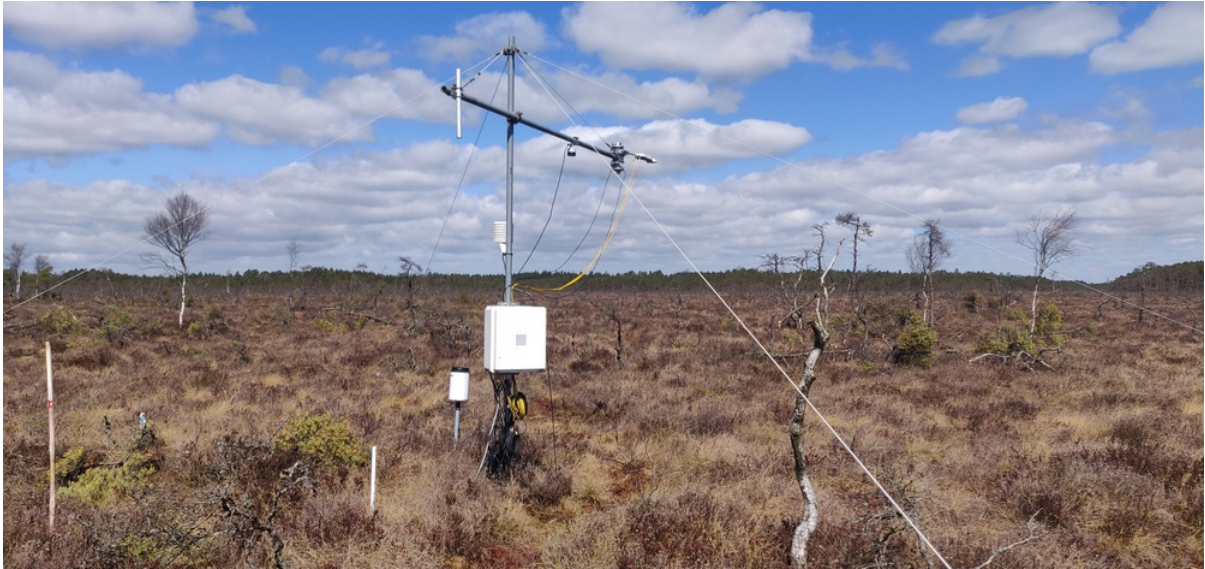Figure A14: To the left: ReefNet Sensus Ultra. To the right: HOBO U20 Water level logger.

Figure A15: The on-site weather station

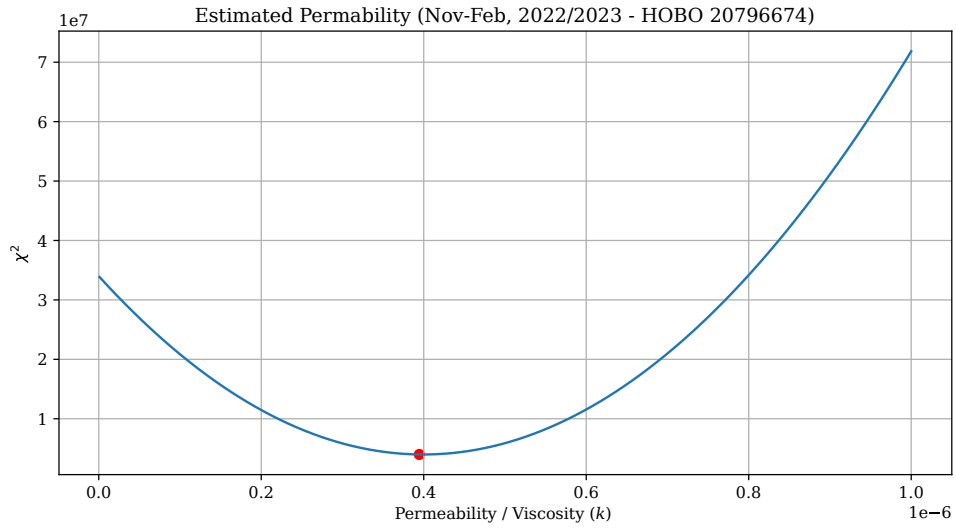Figure A16: The beginning of the tree encroachment

Figure A17: An example of using the chi-squared method to estimate a k value
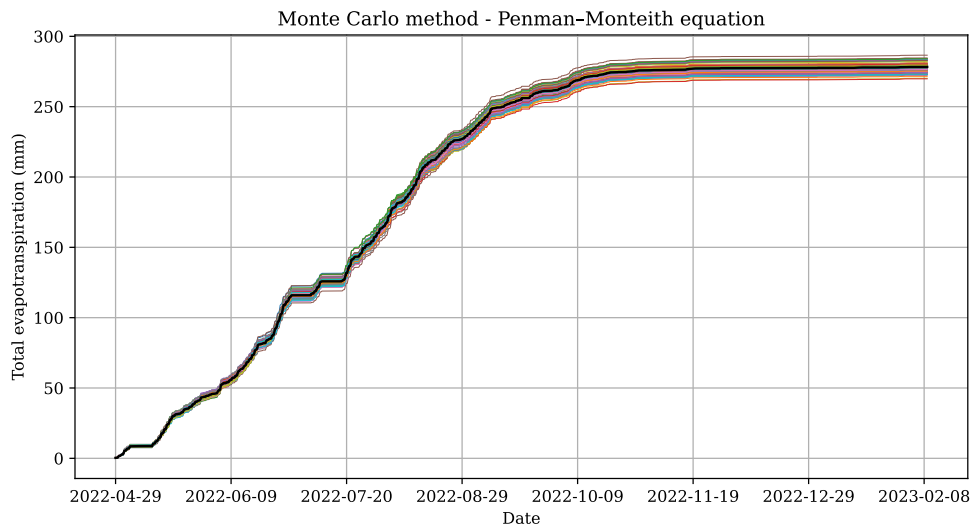

Figure A18: An example of the utilization of the Monte Carlo method on the Penman Monteith equation. The thicker black line represents the mean change.